ALMA MATER STUDIORUM - UNIVERSITÀ DI BOLOGNA

SCUOLA DI INGEGNERIA E ARCHITETTURA

DIPARTIMENTO DI INGEGNERIA INDUSTRIALE

CORSO DI LAUREA IN
INGEGNERIA EDILE-ARCHITETTURA

TESI DI LAUREA

in
Acustica Applicata ed Illuminotecnica

VIBRO-ACOUSTIC CHARACTERIZATION OF CLT PLATES: ANALYTICAL MODEL AND EXPERIMENTAL MEASUREMENT

CARATTERIZZAZIONE VIBRO-ACUSTICA DI LASTRE IN CLT: MODELLI ANALITICI E MISURE SPERIMENTALI

CANDIDATO
Francesco Vagnini

RELATORE:
Chiar.mo Prof. Massimo Garai

CORRELATORI
Prof. Jörn Hübelt
Dr. Ing. Federica Morandi

Anno Accademico 2016/2017
III Sessione

Sommario

Negli ultimi anni i concetti di sostenibilità, elevate efficienze energetiche, rapidità di messa in opera e costi contenuti hanno fatto si che la tecnica costruttiva X-lam (o CLT) riscuotesse successo. L' ingegnerizzazione del materiale conferisce una grande resistenza meccanica all'elemento con spessori ridotti per cui risulta critico l'isolamento acustico. Per questo lo studio del comportamento vibro-acustico dei pannelli in CLT è di estrema importanza. In particolare, risulta importante lo studio del fenomeno della coincidenza, per cui ad una determinata frequenza (la frequenza critica) l'isolamento acustico del solaio, o della parete, diminuisce bruscamente. Per materiali lignei questa frequenza ricade in un intervallo di frequenze in cui la lastra risulta facilmente eccitata dai rumori ambientali. Valutare la frequenza critica comporta dunque lo studio di modelli analitici e sperimentali complessi, per il fatto che il loro comportamento è influenzato dalla naturale caratteristica di ortotropia del pannello. Il lavoro di tesi pertanto riguarda lo studio e l'applicazione di metodi numerici e sperimentali per la valutazione del comportamento acustico di pannelli da costruzione in CLT. La parte introduttiva del lavoro di tesi presenta lo studio del comportamento meccanico e vibratorio di lastre ortotrope. Poi si introduce un parametro fondamentale per la descrizione del campo acustico: l'efficienza di radiazione. Questo parametro descrive il rapporto che sussiste fra il suono irradiato e la velocità di vibrazione della lastra, coniugando cioè l'aspetto acustico e quello meccanico. Per la valutazione del parametro non esiste ancora una procedura standardizzata. Si è fatto quindi riferimento a diverse procedure tratte dalla letteratura scientifica in modo da poter comparare i risultati ottenuti. Sono stati applicati il Discrete Calculation Method (DCM) e la proposta di protocollo sperimentale del CSTB. È stata inoltre studiata la curva di dispersione della lastra. La determinazione sperimentale di tale curva risulta importante per poter dare un'ulteriore validazione ai risultati ottenuti con le misure di efficienza di radiazione ed in tal modo completare lo studio del comportamento vibro-acustico di lastre in CLT. I risultati ottenuti con i diversi metodi mostrano una buona compatibilità sia per il calcolo dell'efficienza di radiazione che per

la valutazione della curva di dispersione. Vengono inoltre sottolieati i limiti e vantaggi dei metodi per la valutazione dell'efficienza di radiazione e curva di dispersione. All'interno dell'appendice vengono confrontati due modelli di valutazione multispettrale della curva di dispersione. Nell'ultima sezione vengono inoltre proposti eventuali sviluppi futuri del lavoro presentato.

Abstract

In the last years, the constructive technique of cross laminated timber (CLT) has received a noticeable success, thanks to contained costs, quickly assemblage and high energetic effciency. Thanks to the great mechanical resistance, the CLT panels are used with moderate thicknesses and therefore relatively little mass, which results critical for acoustic insulation. The study of the acoustic behavior of CLT panels is of extreme importance. The primary interest lies in the study of the phenomenon of the coincidence, for which at one determined frequency (the critical frequency) the acoustic insulation of the construction element (wall/floor) brusquely decreases. For CLT elements this frequency falls into an interval of frequencies in which the plate is easily excited by the environmental noises. The appraisal of the critical frequency involves, therefore, the study of analytical and experimental complex models, for the fact that their behavior is infuenced by the natural orthotropic characteristic of the panel. The main task of thesis therefore concerns the study and the application of analytical and experimental methods for the evaluation of the acoustic behavior of CLT panels. The introduction of thesis concerns the study of the mechanical and vibrational behavior of orthotropic plates. Then a fundamental parameter is introduced for the description of the acoustic field: the radiation efficiency. This parameter describes the relationship that subsists between the radiated sound power and the velocity of vibration of the plate, conjugating the acoustic and the mechanic aspects. Therefore reference is made to different procedures drawn by the scientific literature that allow to compare different results. The Discrete Calculation Method (DCM) and the experimental protocol proposed by CSTB have been applied. The dispersion curves of the plate have been studied besides; the experimental determination of such curve results important to be able to give a further validation to the results achieved with the measurements of radiation efficiency and in such way to complete the study of the vibro-acoustic behavior of CLT plates. The results obtained with the different methods show a good agreement both for the calculation of the radiation effciency and for the evaluation of the dispersion curves.

Contents

Chapter 1

Introduction

Great mechanical resistance with moderate thicknesses, and therefore relatively little mass, make the CLT panels critical for acoustic insulation. The coincidence phenomena determine a decrease of the acoustic insulation of the construction element (wall/floor), moreover it identifies the limit of different sound radiation regimes. For CLT elements this frequency falls into an interval of frequencies in which the plate is easily excited by the environmental noises. The appraisal of the critical frequency involves, therefore, the study of analytical and experimental complex models, for the fact that their behavior is influenced by the natural orthotropic characteristic of the panel. The introduction of thesis concerns the study of the mechanical and vibrational behavior of orthotropic plates: the theory of structure-borne sound and the vibration fields related to it are introduced. Three kinds of waves propagate in solids: quasi-longitudinal, shear and bending waves. Due to the greater out of plane displacement, the responsible of the radiated sound power are the bending waves. Bending waves are dispersive, i.e. their velocity is frequency dependent, rather than shear and quasi longitudinal. The dispersion of bending waves is related to the characteristics of the solid investigated; knowing the dispersion curve, the behavior of the element can be defined. Thus the first approach to the problem is the study of the bending wave motion on one direction and then the study is extended to homogeneous and orthotropic plates. Once the behavior of the element is known, it is important to evaluate and describe how mechanical vibration are converted into sound power. The parameter conjugating the acoustic aspect with the mechanic behavior is the radiation efficiency, expressed as a ratio between the effective and theoretical radiated sound power.

The first part of the thesis is focused on evaluation of the radiation efficiency and the second part on the estimation of the dispersion curves, in order to have a deeper understanding of wave propagation into the element.

The theoretical approach for the study of radiation efficiency takes into account the modal analysis of the plate. It is assumed that the radiated sound power is due to the resontant modes, therefore for a non-resonant mode no sound power is radiated. Modal sound radiation can be evaluated either with Rayleight integral [1] or with Leppington's approach [2], knowing the chacracteristic of the element and the boundary condition. Anyhow, for finite thin plates undergoing determied assumption, numerical approximation formulas are shown.

As it concerns the experimental approach, two procedures suggested by literature are taken into account in order to have a comparison between the results: the Discrete Calculation Method (DCM) and the proposal of CSTB. The Discrete Calculation Method subdivides the plate into a grid of elements in which the vibration velocity is measured. The elements are supposed to be a circular piston having the same equivalent area and vibrating with the measured velocity. Thus summing up and averaging the resulting radiated sound power of each element, radiation efficiency can be evaluated. The CSTB proposal evalutes the radiation efficiency through the measurement of sound reduction indices, impact sound insulation levels and vibration velocity levels. It's execution needs acoustic transmission chambers, where the velocity level of the vibrating plate is evaluated at the surface and the sound pressure field is averaged in the receiving room: by combining this data, radiation efficiency can be found. The approach is quite simple and measurement can be done easly, but standardised testing facilities are needed because the sound response of the receiving room can influence the results. To evaluate the dispersion curves, means to find the wavenumbers as function of frequency. This relationship, that is proper of the material, allows us to understand the behavior of the element. More algorhitms are take into account to estimate the curve that can be subdivided into two categories: mono and plurispectral methods. Monospectral algorhitms find at first the time of flight between to subsequent accelerometers, then the phase velocity is determined knowing the distance between the accelerometers. The multispectral analysis find a image dispersion from which the dispersion curve is evaluated.

The main task of thesis therefore concerns the study of all the theoretical models briefly listed above, the implementation of the algoritms for the determination of the radiation efficiency and the dispersion curves, and finally the validation through experimental measurements of the methodologies that proposed by the reference literature.

Chapter 2

Background theory

The aim of this chapter is to introduce the vibro-acoustic behavior of structures,in particular the so called structure-borne sound. Many sound events are produced or conducted by vibrating solid bodies that radiate sound power into adjoining ambient. The following chapter will briefly introduce the wave propagation theory for homogeneous isotropic and orthotropic plate and provide a detailed description of one of most important parameters in this field: the radiation efficiency.

2.1 Vibrational fields

The relation between displacement $\eta(t)$, velocity $v(t)$ and acceleration $a(t)$ may be written as:

$$v(t) = \frac{d\eta(t)}{dt} \qquad a(t) = \frac{dv(t)}{dt} = \frac{d^2\eta(t)}{dt^2} \tag{2.1}$$

Vibration can involve different medium such as gas, fluid or solid. The difference between the chemical bond constituent the medium demonstrate the fact that fluid or gas cannot transfer share motion to adjoining region while, solids can assume a bendable shape due to its micro-structure [3]. So structure-motion can be described by composing three types of waves:

- quasi-longitudinal waves
- transverse shear waves
- bending waves

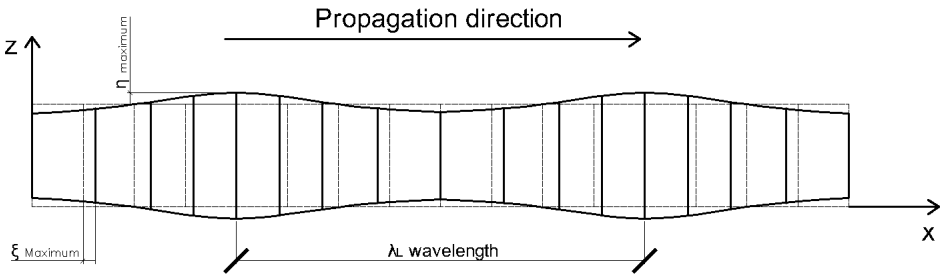

Figure 2.1: Quasi-longitudinal wave propagation

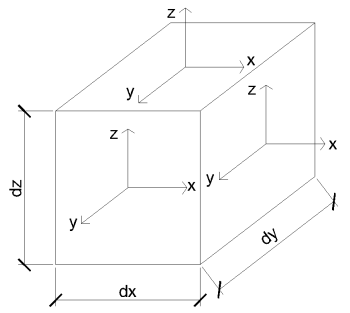

Figure 2.2: Element of a plate

2.1.1 Quasi-longitudinal waves

Quasi-longitudinal waves are a subset of pure longitudinal waves in which the propagation is in the same direction as the particle motion. The propagation causes a compressed and decompressed region in the plate, thus due to the limited dimension of the element even lateral strains take place. Considers a plate divided into n-element as shown in the Fig. 2.1: it can be easily seen how the lateral strain takes place while the wave is propagating in the x-axis, due to the Poisson's law. Consider one of the elements of the above-illustrated plate, Fig. 2.2 referring the axis as the picture. The general set of equations relating Young's modulus and Poisson's ratio to stress and strain are:

$$\epsilon_x = \frac{1}{E}\left[\sigma_x - \nu\left(\sigma_y + \sigma_z\right)\right] \tag{2.2}$$

$$\epsilon_y = \frac{1}{E}\left[\sigma_y - \nu\left(\sigma_x + \sigma_z\right)\right] \tag{2.3}$$

$$\epsilon_z = \frac{1}{E}\left[\sigma_z - \nu\left(\sigma_y + \sigma_x\right)\right] \tag{2.4}$$

where ϵ_i is the deformation among i- axis, E is the Young's modulus, ν is the Poisson's ration and σ_i is the stress among i-axis. In the quasi-longitudinal wave, there are no cross-sectional contraction, namely for:

$$\epsilon_y = 0; \qquad \sigma_z = 0 \tag{2.5}$$

Eq. (2.3) gives:

$$\sigma_y = \nu\sigma_x \tag{2.6}$$

and substituted into Eq.(2.2) Eq. (2.3) Eq. (2.4):

$$\epsilon_x = \frac{1}{E}\sigma_x\left(1-\nu^2\right) \tag{2.7}$$

where $\frac{E}{1-\nu^2}$ can be though as an effective Young's modulus. For dynamic equilibrium, the strain and stress are linked by:

$$\frac{\partial\sigma_x}{\partial x} = \rho\frac{\partial^2\epsilon_x}{\partial t^2} \qquad or \qquad \frac{\partial\sigma_x}{\partial x} = \rho\frac{\partial v_x}{\partial t} \tag{2.8}$$

by substituting equation (2.7) into (2.8), the quasi-longitudinal waves equation may be written as:

$$\frac{E}{1-\nu^2}\frac{\partial^2\epsilon_x}{\partial x^2} - \rho\frac{\partial^2\epsilon_x}{\partial t^2} = 0 \tag{2.9}$$

taking the solution:

$$\epsilon(x,t) = \epsilon_0 e^{i(\omega t - k_x x)} \tag{2.10}$$

the longitudinal wave velocity is:

$$c_L = \sqrt{\frac{E}{\rho(1-\nu^2)}} \tag{2.11}$$

2.1.2 Transverse waves

Solids do not only resist changes in volume, they also resist changes in shape thus transverse waves can propagate due to solids capacity to support shear stresses. The displacement occurs on the plane having the propagation axis as normal vector, so referring to Fig. 2.2, taking x-axis as propagation direction and studying the motion in the y axis, the shear deformation is shown in Fig. 2.3.

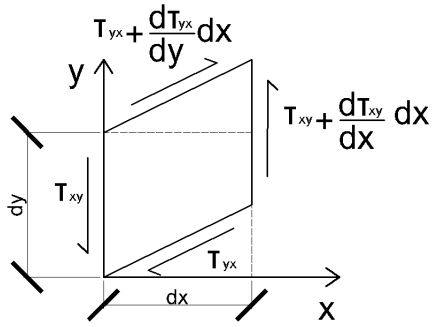

Figure 2.3: Tangential stresses from the element of a plate

where:

$$\gamma_{xy} = \frac{\partial \eta}{\partial x} \tag{2.12}$$

where γ_{xy} is the angle defined after the shear deformation, therefore transverse waves are also known as rotational waves. Knowing the general equation relating stress and strain:

$$\tau_{xy} = \tau_{yx} = G\gamma_{xy} = G\frac{\partial \eta}{\partial x} = G\frac{\partial v_y}{\partial x}\partial t \tag{2.13}$$

where G is the shear modulus τ_{xy} is the tangential stress. For dynamic equilibrium it has to be satisfied:

$$\frac{\partial \tau_{xy}}{\partial x} = \rho\frac{\partial v_y}{\partial t} \tag{2.14}$$

substituting equation (2.13) into (2.14) propagation velocity can be found:

$$c_T = \sqrt{\frac{G}{\rho}} = \sqrt{\frac{E}{2\rho(1+\nu)}} = \sqrt{\frac{1-\nu}{2}}c_L \tag{2.15}$$

2.1.3 Bending waves

Bending waves, also knows as flexural waves, are the most relevant for sound radiation of plates or beams. Comparing the deflection among the three above mentioned waves, flexural ones display the most prominent displacement thus the majority sound radiation is associated to these waves. Bending waves cannot be classified as transverse waves, both because the stress and strain that dominate the potential energy are acting in different direction,

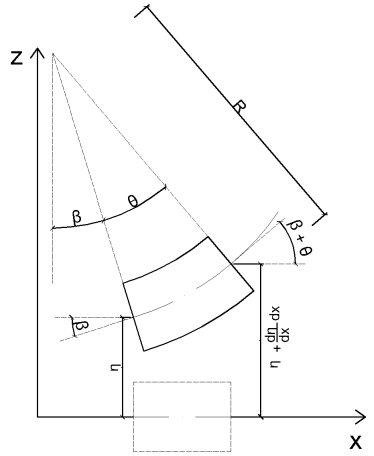

Figure 2.4: Relation between displacement and rotation

and because the entire behavior and the describing waves-motion equation differ greatly from the other two mentioned above. Further considerations about the mechanical conservation of bending waves can be found in [3]. Taking into account the Eulero-Bernoulli hypothesis, Kirchhoff's theory gives a description of propagating bending waves equation in therms of four variables: transverse velocity v_z, angular velocity ω_y, bending moment M_y and shear force F_z transmitted across the section. Referring to Fig 2.4, we can define:

$$\beta = \frac{\partial \eta}{\partial x} \qquad \omega_y = \frac{\partial \beta}{\partial t} = \frac{\partial^2 \eta}{\partial t \partial x} = \frac{\partial v_z}{\partial x} \tag{2.16}$$

If the rotatory inertia of the element is ignored, under the assumption of acoustic thin plate [3], the dynamic equilibrium on the z-axis may be written as:

$$\frac{\partial F_z}{\partial x} = -\rho_s \frac{\partial^2 \eta}{\partial t^2} \tag{2.17}$$

where $\rho_s = \rho h$ is the mass per unit area, for equilibrium need to be satisfied:

$$F_z = -\frac{\partial M_y}{\partial x} \tag{2.18}$$

moreover from Navier's equation moments can be seen as:

$$M_y = -\frac{EI}{1-\nu^2}\frac{\partial^2 \eta}{\partial x^2} = B\frac{\partial^2 \eta}{\partial x^2} \tag{2.19}$$

where $B = -\frac{EI}{1-\nu^2}$; by substituting (2.19) into (2.18) into (2.17) free-vibration[1]

[1]The hypothesis of free-vibration is made possible considering a uniform flat plane of infinite extent

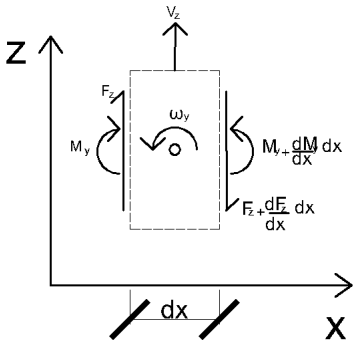

Figure 2.5: Transverse velocity v_z, angular velocity ω_y, moments M_y, shear force F_z

equation may be written as:

$$B\frac{\partial^4 \eta}{\partial x^4} = -\rho_s \frac{\partial^2 \eta}{\partial t^2} \tag{2.20}$$

finally assuming the following free-wave solution:

$$\eta(x,t) = \eta_0 e^{i(\omega t - k_x x)} \tag{2.21}$$

substituting into (2.20) gives:

$$k_x^4 = k_B^4 = \frac{\omega^2 \rho_l}{B_b} \tag{2.22}$$

where k_B is the structural wavenumber. Knowing the relation between wave number and angular frequency, phase velocity can be found:

$$c_\phi = \frac{\omega}{k} \qquad\qquad c_B = \sqrt[4]{\frac{B}{\rho_s}}\sqrt{\omega} = \sqrt{\frac{2\pi f h c_L}{\sqrt{12}}} \tag{2.23}$$

where c_B is the bending velocity,h is the thickness of the plate, c_L is the longitudinal wave and f is the frequency. It needs to underlined that the velocity of bending waves is a function of frequency where each frequency component of waveform propagates with a different phase velocity. Moreover the bending stiffness B refers to the material elastic property, so different solids imply different phase velocities as a function of frequency. The relation between frequencies and each corresponding phase velocity is called dispersion curve.

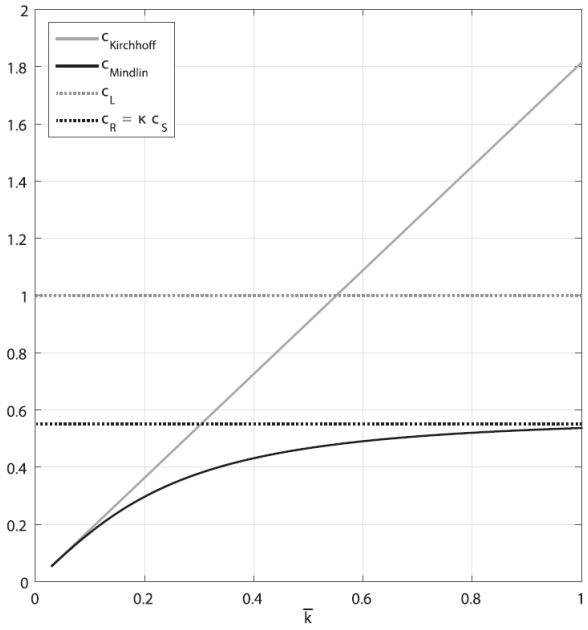

Figure 2.6: Comparison of wave velocity

Fig. 2.6 shows how shear, longitudinal and bending wave speed are related with the frequency. However the equation (2.20) refers to a one-direction propagation, x-axis, whereas in plates two dimensional bending wave-fields occur simultaneously. Next section will describe a complete derivation of bending wave equation in which at first rotatory inertia and shear deformation are neglected - Kirchhoff's theory of thin plate - and then acoustical thick plate - Mindlin's theory - will be considerd.

2.2 Structure-borne sound in homogeneous isotropic plate

Kirchhoff's plate theory, considered an extension of Euler-Bernoulli beam theory, assumes the axial deformation of the plate thickness negligible and the plane section remaining perpendicular to the middle plan after deformation. In acoustics, thin plates are considered when the wavelength is large compared to the thickness of the plate thus shear deformation can be neglected. For a free vibration and plane-progressive wave, Eq. (2.20) becomes:

$$\frac{\partial^4 \eta}{\partial x^4} + 2\frac{\partial^4 \eta}{dx^2 dy^2} + \frac{\partial^4 \eta}{\partial y^4} - \frac{\rho_s}{B}\omega^2 \frac{\partial^2 \eta}{\partial t^2} = 0 \tag{2.24}$$

hence for a forced vibration it becomes:

$$\frac{d^4\eta}{dx^4} + 2\frac{d^4\eta}{dx^2dy^2} + \frac{d^4\eta}{dy^4} - \frac{\rho_s}{B}\omega^2\frac{\partial^2\eta}{\partial t^2} = \frac{j\omega p}{B'} \tag{2.25}$$

where p denotes an external force of area acting on the plate; ρ_s represents the mass per unit area, B is the stiffness matrix, v is the vibration velocity and η is the displacement among z-axis
The solution:

$$\eta(x, y, t) = \eta_0 e^{i(\omega t - k_x x - k_y y)} \tag{2.26}$$

where η_0 is an arbitrary constant, and k_x k_y are constant in which substituting (2.26) into (2.24):

$$k_B = k_x^2 + k_y^2 \tag{2.27}$$

where k_B is the bending wavenumber, k_x is the wavenumber among x-axis k_y is the wavenumber among y-axis. Considering a simply supported plate (in which thickness is developed on z-axis) as a combination of two beams: one aligned on x-axis and the other on y-axis, phase closure (or mode frequencies) occurs when:

$$k_B^2 = \left(\frac{m\pi}{L_x}\right)^2 + \left(\frac{n\pi}{L_y}\right)^2 \tag{2.28}$$

which implies that bending mode frequencies for simply supported isotropic rectangular plates can be calculated from Eq. (2.28), and (2.22) as:

$$f_{m,n} = \frac{c_B}{2}\sqrt{\left(\frac{m}{L_x}\right)^2 + \left(\frac{n}{L_y}^2\right)} \tag{2.29}$$

2.3 Structure-borne sound in orthotropic materials

In solids orthotropic materials have different properties along two orthogonal directions which imply different sound propagation characteristics as a function of the angle between the direction considered and the principal axis.

Kirchhoff's theory - thin orthotropic plate

The equation of motion of a thin orthotropic plate can be derived by the Kirchhoff's theory, using Euler-Bernoulli hypothesis:

$$D_x\frac{d^4\eta}{dx^4} + 2B\frac{d^4\eta}{dx^2dy^2} + D_y\frac{d^4\eta}{dy^4} = \rho h\frac{d^2\eta}{dt^2} \tag{2.30}$$

where:

$$D_x = \frac{E_x}{12(1-\nu^2)} \tag{2.31}$$

$$D_y = \frac{E_y}{12(1-\nu^2)} \tag{2.32}$$

$$B = \frac{\nu_x D_x}{2} + \frac{\nu_y D_x}{2} + \frac{G_{xy}}{12}h^3 \sim \sqrt{D_x D_y} \tag{2.33}$$

η represents z-axis displacement, D represents the bending stiffness among the subscript axis, and B the torsional stiffness. The equation (2.33) can be simplified assuming the shear modulus G_{xy} as a function of the two Young's modulus in the principal directions E_x E_y and the Poisson's ratio:

$$G_{xy} = \frac{\sqrt{E_x E_y}}{2(1+\sqrt{\nu_{xy}\nu_{yx}})} \tag{2.34}$$

The wave-number is assumed to be independent among the principal direction,$k_{B,x}$ $k_{B,y}$ rather than every others direction that can be described with the elliptic model:

$$k_{B,\theta}(\omega,\theta) = \sqrt{k_{B,x}^2(\theta) + k_{B,y}^2(\theta)} \tag{2.35}$$

where:

$$k_{B,x} = \sqrt{\omega}\sqrt[4]{\frac{\rho h}{D(\theta)}}\cos\theta \tag{2.36}$$

$$k_{B,y} = \sqrt{\omega}\sqrt[4]{\frac{\rho h}{D(\theta)}}\sin\theta \tag{2.37}$$

with the analogy of wave-numbers in homogeneous material, it is possible to describe $k_{B,\theta}$ in terms of angular frequencies ω and θ angle (between x-axis and general directions):

$$k_B^4(\omega,\theta) = \frac{\rho h}{D(\omega,\theta)}\omega^2 \tag{2.38}$$

Bending stiffness as a function of θ and ω is defined as:

$$D(\omega,\theta) = D_x(\omega)\cos^4\theta + 2B(\omega)\cos^2\sin^2\theta + D_y(\omega)\sin^4\theta \tag{2.39}$$

this requires the knowledge of the shear modulus in plane G_{xy}.
Furthermore, knowing that the resonant mode occurs when:

$$k_B^2 = \left(\frac{m\pi}{L_x}\right)^2 + \left(\frac{n\pi}{L_y}\right)^2 \tag{2.40}$$

where L_x and L_y are the dimension of the plate, m and n are natural number. The bending mode frequencies for a simply supported orthotropic rectangular plates are:

$$f_{m,n} = \frac{\pi}{2\sqrt{\rho_s}}\left[\sqrt{D_x}\left(\frac{m}{L_x}\right)^2+\sqrt{D_y}\left(\frac{n}{L_y}\right)^2\right] = \frac{\pi h}{2\sqrt{12}}\left[c_{L,x}\left(\frac{m}{L_x}\right)^2+c_{L,y}\left(\frac{n}{L_y}\right)^2\right] \tag{2.41}$$

where $c_{L,x}$, $D_{L,y}$ are the quasi-longitudinal velocity among x and y-axis.

Mindlins theory - thick orthotropic plate

The limit of Kirchhoff theory lies on the thickness of the medium studied, therefore when the assumption of thin layer is not valid, it is possible to consider the Mindlins and Reissner's theory. This formulation take in account the shear deformation and the rotatory inertia and thus the elastic constants can be determinated without considering the frequency dependence. With Eulero-Bernoulli Hypothesis named h the thickness of the plate Mindlins equation is:

$$D\nabla^4\eta - \left[\frac{\rho D}{\kappa G} + I\right]\nabla^2\frac{\partial^2\eta}{\partial t^2} + \rho\frac{I}{\kappa^2 G}\frac{\partial^4\eta}{\partial t^4} + \rho h\frac{\partial^2\eta}{\partial t^2} = 0 \tag{2.42}$$

where G is the shear modulus, and κG can be considered as the "effective" shear modulus, meanwhile κ is analog to Timoshenko's coefficent, that considers the changed of shear stress over the plate thickness and I is the inertia of the plate. κ can be approximated as:

$$\kappa = \frac{c_r}{c_s} = \frac{0.87 + 1.12\nu}{1+\nu} \tag{2.43}$$

where ν is the Poisson's ratio, c_S is the shear wave velocity and c_R is the Rayleigh surface velocity. Mindlin's dispersion relation is calculate as follow:

$$\left(1 - \frac{c_B^2}{\kappa^2 c_S^2}\right)\left(\frac{c_L^2}{c_T^2} - 1\right) = \frac{12}{h^2\left(\frac{\omega}{c}\right)^2} \tag{2.44}$$

The solution may be written in the of displacement as:

$$\eta(x,t) = Ae^{i(\omega t - k_x x)} \tag{2.45}$$

and the wave number that allows to satisfy the equation is the solution to:

$$k_x^4 - k_x^2\left(k_l^2 + \frac{k_t^2}{T}\right) - \left(k_b^4 - \frac{k_l^2 k_t^2}{T}\right) = 0 \tag{2.46}$$

where the longitudinal wavenumber is:

$$k_l = \omega\sqrt{\frac{\rho}{E}}$$

the wavenumber for transverse waves:

$$k_l = \omega\sqrt{\frac{\rho}{G}}$$

the wavenumber for longitudinal waves:

$$k_l = \frac{\mu\omega^2}{D_b^{\frac{1}{4}}}$$

Thus theories allow to determine wave dispersion relation, in an elastic orthotropic element, from the equation of motion of the vibrating structure. Assumptions of thin plates are generally satisfied by the relation:

$$\lambda_b > 2\pi h \tag{2.47}$$

In case this condition is not met, rotational inertia and shear deformation have significant effects and Mindlin's theory needs to be considered.
In this case analytical solutions may not be computed, in fact comparing equation (2.27) with (2.46) we can see that it is no longer possible to consider the bending wave-number as a sum of k_x and k_y, thus values of resonant frequencies can be obtained knowing the bending wave-number and the corresponding plate resonant frequency assuming the plate as thin.

2.4 Radiation efficiency

The radiation efficiency is one of the parameters used to characterize the sound property of elastic plates and it relates the sound radiation to the vibrating velocity. The aim of this parameter is to describe how a plate, under its own boundary conditions, can convert structure-borne vibrations into sound power into the adjoining fluid. Other parameters can be used to describe the phenomena such as *sound power*, in this case of a vibrating plate the sound power produced by the plate depends upon the method of excitation of vibration, the dimension and the material including damping of plate. Sound radiation efficiency, in particular for a specific mode, is independent of amplitude and method of excitation. Once we know the relation between the sound power transmitted and vibration velocity, we can

estimate the noise or sound radiation and thus implement any subsequent sound/noise control mitigation action.
The radiation efficiency is directly connected to a *radiation resistance* trough the area of the plate and the specific acoustic resistance of the fluid:

$$\sigma(\omega) = \frac{W_{rad}(\omega)}{\rho_0 c_0 S \langle v^2 \rangle} = \frac{R_{rad}(\omega)}{\rho_0 c_0 S} \tag{2.48}$$

where $\langle v^2 \rangle$ is the space-time average of squared vibration velocity of the plate, W_{rad} is the time-average pressure sound power radiated by the panel, ρ_0, c_0 the density and speed velocity of air. Thus the radiation efficiency can be seen as the ratio between the sound power actually radiated by the surface of the plate and the theoretical sound power radiated by a piston source having the same surface area and vibration velocity of the plate. Two main expressions can be adopted to estimate the modal sound radiation, one is Leppington theory using the asympthotic assumption and the other is Rayleigh integral [1].

2.4.1 Infinite plate

Once analyzed an infinite extended plate vibrating - ideal case - it is possible to compute the radiation efficiency from more complicated finite system. Further it is useful to consider, as first explanation, sound radiation of a plate with null damping factor thus is possible to simplify modal analysis due to the linear independence between the two degree freedom system. As already commented, the bending velocity of x-directional propagating vibration is given by:

$$v(x,t) = v_0 e^{i(\omega t - k_B x)} \tag{2.49}$$

The radiated sound pressure propagating has the following structure:

$$p(x,z,t) = p_0 e^{i(\omega t - k_B x - k_z z)} \tag{2.50}$$

wave equation in fluid in therm of wave-number may be written as:

$$\frac{\partial^2 p}{\partial x^2} + \frac{\partial^2 p}{\partial y^2} + \frac{\partial^2 p}{\partial z^2} - k^2 p = 0 \tag{2.51}$$

Hence from Eq. (2.50) and (2.51) it follows:

$$k^2 = k_B^2 + k_z^2 \tag{2.52}$$

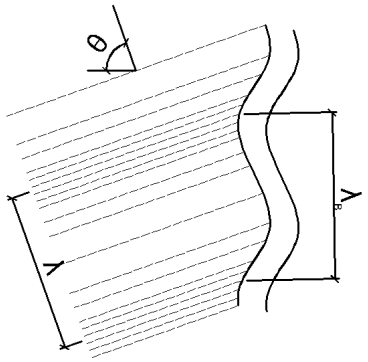

Figure 2.7: Plane wave radiated into environment by bending wave in a plate above the critical frequency

where k represents the ambient wave number k_B the bending wave-number. Moreover it is important to underline that velocity at plate surface must be equal to the velocity of the adjacent fluid, this implies:

$$v(x,t) = u_z(x,t) \qquad for \qquad z = 0 \tag{2.53}$$

remembering that for airborne sound velocity is related to pressure under the equation:

$$v_{z=0} = -\frac{1}{i\omega\rho}\left(\frac{\partial p}{\partial z}\right)_{z=0} = p_0 \frac{k_z}{\omega\rho_0} e^{-ik_B x} \tag{2.54}$$

hence radiated sound pressure must be:

$$p(x,z,t) = \frac{v_0\rho_0\omega}{\sqrt{k_B^2 - k^2}} e^{i(\omega t-(k+k_B)z)-k_B x} \tag{2.55}$$

where ρ_0 is the air density, ω the angular frequency,v vibration velocity As it possible to see in Eq. (2.54), sound pressure in the adjacent fluid is described by two cartesian axes, thus it is possible represent wave in 2-d form.
If we define θ as:

$$\sin\theta = \frac{k_B}{k} \tag{2.56}$$

equation (2.54) can be rewritten :

$$p(x,z,t) = \frac{v_0\rho_0 c_0}{\cos\theta} e^{i(\omega t-(k+k_B)\cos\theta)-k_B\sin\theta)} \tag{2.57}$$

the other mathematically solution $e^{+\sqrt{k_B - k^2}z}$ is ruled out on the basis of energy considerations.

Two different regimes can be noted, one above critical frequency and the other below. It must be explained that critical frequency is defined as the frequency in which acoustic wavelength is equal to the bending wavelength. Therefore looking at equation(2.56), for critical frequencies it occurs:

$$\lambda = \lambda_B \qquad k = k_B \qquad c_0 = c_B \tag{2.58}$$

The aforementioned equations all refer to the above critical frequency regime. Referring at the case:

$$\lambda_B > \lambda \tag{2.59}$$

Further observing Eq. (2.56) θ assumes real values and also radiate waves that propagate parallel to the plate. In here bending velocity waves are in-phase with the ambient, or adjoining fluid, and looking at equation (2.54) the wave-number z assumes real values

$$k_z = Re[k_z] \tag{2.60}$$

remembering the wave number relation:

$$k_z = \sqrt{k^2 - k_B^2} \tag{2.61}$$

Real values of k_z mean that the sound can propagate away from the plate and mechanical pressure is transferred from the vibrating plate to the adjacent fluid. The radiation efficency may be written as:

$$\sigma = \frac{1}{\cos\theta} = \frac{k}{\sqrt{k^2 - k_B^2}} \tag{2.62}$$

assuming the plate as very large plane rather than infinite thus surface have a finite[2]value. The regime below critical frequency regime occurs when:

$$\lambda_B < \lambda \tag{2.63}$$

Thus wave number k_z assumes a imaginary value:

$$k_z = Im[k_z] \tag{2.64}$$

thus no mechanical pressure is transferred to the adjacent fluid, demonstration of it lying on the shift phase angle at the plate surface equal to 90^o, so radiation power has null value as result. Pressure and velocity have steep exponential decays and the to component of velocity may be written as:

$$u_x(x,z,t) = \frac{ik_B v_0}{\sqrt{k_B^2 - k^2}} e^{i[\omega t - (z\sqrt{k_b^2 - k^2} + k_B x)]} \tag{2.65}$$

[2]We assume that S is not an infinite surface but have a great value so $W = \frac{S\rho_0 c_0 v^2}{2\cos\theta}$

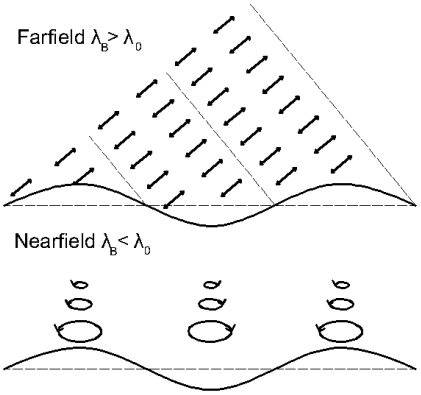

Figure 2.8: Particle motions in far field and near field radiation

$$u_x(x,z,t) = v_0 e^{i[\omega t - (z\sqrt{k_b^2 - k^2} + k_B x)]} \tag{2.66}$$

The motion in this case describes an ellipse, as Brillouin demonstrated [4]. An easily way to overlook this phenomena is to describe it through simple practical example: if we try to make water-wave during a sea-bath shaking one hand slowly, no wave will be made, because hands do not have enough area to create a variation of volume, but using all of the arm rather the only hand, you will be able to create a wave, and its can propagate away from your body. Fig. 2.8 shows the motion of the particles in a plate.

2.4.2 Finite plate

Considering a finite plate, is possible to sketch it as array of source points in which the resulting radiation is the same from flexural vibration of a rectangular plate. Dividing the plate by the nodal lines and assuming each element as a point source in the same phase, rectangular plate can be represent by the following picture:

With reference to Fig. 2.10, a point in the ambient field can be described as a function of two angles and one linear coordinate. At any angular frequency ω the sound pressure can be calculated for a single coupled mode in

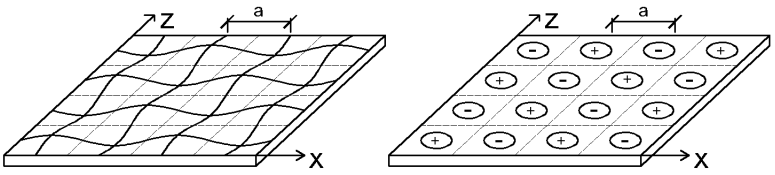

Figure 2.9: Plate sub-dividing of simple point source

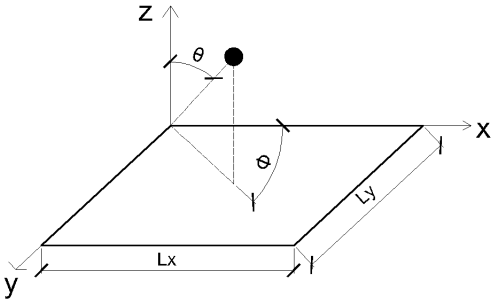

Figure 2.10: Cylindrical coordinate

the far field[3] as:

$$p_{m,n}(r,\theta,\phi,t) = \frac{i\omega\rho_0}{2\pi r}e^{i(\omega t-kr)}\int_0^{L_x}\int_0^{L_y} v_{m,n}\psi_{m,n}e^{i[(\frac{kL_x\sin\theta\cos\phi x}{L_x}+\frac{L_x\sin\theta\sin\phi y}{L_y})]}dxdy \tag{2.67}$$

where $\psi_{m,n}$ is the mode shape, $v_{m,n}$ is a constant relating to the velocity in the z-direction:

$$\psi_{m,n} = \sin\left(\frac{m\pi x}{L_x}\right)\sin\left(\frac{n\pi z}{L_y}\right) \tag{2.68}$$

and velocity for a (m,n)-mode may be written:

$$v(x,z) = v_{m,n}\sin\left(\frac{m\pi x}{L_x}\right)\sin\left(\frac{n\pi z}{L_y}\right) \qquad for \qquad 0<x<a \qquad 0<z<b \tag{2.69}$$

[3]far field is considered when the position vector of the point considered is much larger than the dimension of the plate: $R >> L_x \quad R >> L_y$

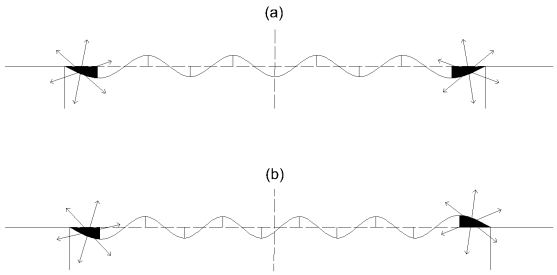

Figure 2.11: Symmetric odd mode (a) and even mode (b)

Knowing the pressure, sound intensity can be calculated as:

$$I_{m,n}(r,\theta,\phi) = \frac{1}{T}\int_0^T p(r,\theta,\phi,t)v(r,\theta,\phi,t)dt \tag{2.70}$$

The sound intensity vector is radially direct in the far field due to the in phase velocity of the particle and the pressure radiated. As a result, for harmonic vibration, the intensity vector can be calculated as:

$$I_{m,n}(r,\theta,\phi) = \frac{1}{2}Re\Big[p(r,\theta,\psi,\omega)v(r,\theta,\psi,\omega)\Big] = \frac{|p(r,\theta,\psi,\omega)|^2}{\rho_0 c_0} \tag{2.71}$$

thus substituting (2.67) into (2.71), radiation intensity is given by:

$$I_{m,n}(r,\theta,\phi) = 2\rho_0 c_0 \left(\frac{v_{m,n}kL_XL_y}{r\pi^3 mn}\right)^2 \left[\frac{\Gamma\left(\frac{kL_x\sin\theta cos\theta}{2}\right)\Lambda\left(\frac{kl_y\sin\theta\sin\phi}{2}\right)}{\left[\left(\frac{kL_x\sin\theta cos\theta}{m\pi}\right)^2-1\right]\left[\left(\frac{kl_y\sin\theta\sin\phi}{n\pi}\right)^2-1\right]}\right]^2 \tag{2.72}$$

where Γ is *cos* when p is an odd integer and *sin* when p is an even integer(see Fig. 2.11): thus the power radiated from the plate is:

$$P_{m,n} = \int_0^{2\pi}\int_0^{\frac{\pi}{2}} I_{m,n}(r,\theta,\phi)r^2\sin\theta d\theta d\phi \tag{2.73}$$

Known the average radiation efficiency of the mode, velocity averaging for each single mode must be made; considering an appropriate period T:

$$\left\langle v_n^2\right\rangle_{t,S} = \frac{1}{S}\int_S \frac{1}{T}\int_0^T v_n(x,z)dtds \tag{2.74}$$

where S is the surface. Hence the radiation efficiency $\sigma_{m,n}$ for the (m,n) mode can be defined:

$$\sigma_{m,n} = \frac{64k^2L_xL_y}{\pi^6m^2n^2}\int_0^{\frac{\pi}{2}}\int_0^{\frac{\pi}{2}}\left\{\frac{\Gamma\left(\frac{kL_x\sin\theta cos\theta}{2}\right)\Lambda\left(\frac{kl_y\sin\theta\sin\phi}{2}\right)}{\left[\left(\frac{kL_x\sin\theta cos\theta}{m\pi}\right)^2-1\right]\left[\left(\frac{kl_y\sin\theta\sin\phi}{n\pi}\right)^2-1\right]}\right\}^2\sin\theta d\theta d\phi \tag{2.75}$$

It is important to remember that the above illustrate equation undergo the assumption of far field:

$$R >> L_x \qquad R >> L_Y \tag{2.76}$$

Numerical approximation of Eq.(2.76) are made by Wallace [5]:

for $kL_x << 1$ and $kL_Y << 1$

$$\sigma_{m,n} = \frac{32k^2L_xL_y}{\pi^5m^2n^2}\left\{1-\frac{k^2L_xL_y}{12}\left[\left(1-\frac{8}{(m\pi)^2}\right)\frac{L_x}{L_y}+\left(1-\frac{8}{(n\pi)^2}\right)\frac{L_y}{L_x}\right\} \tag{2.77}$$

when p and q are both odd integers

$$\sigma_{m,n} = \frac{2k^6L_x^3L_y^3}{15\pi^5m^2n^2}\left\{1-\frac{5k^2L_xL_y}{64}\left[\left(1-\frac{24}{(m\pi)^2}\right)\frac{L_x}{L_y}+\left(1-\frac{24}{(n\pi)^2}\right)\frac{L_y}{L_x}\right\} \tag{2.78}$$

when p and q are both even integers

$$\sigma_{m,n} = \frac{8k^4L_xL_y^3}{3\pi^5m^2n^2}\left\{1-\frac{k^2L_xL_y}{20}\left[\left(1-\frac{8}{(m\pi)^2}\right)\frac{L_x}{L_y}+\left(1-\frac{24}{(n\pi)^2}\right)\frac{L_y}{L_x}\right\} \tag{2.79}$$

In Fig 2.12 an example of radiation efficiency is shown for building acoustic frequency range: it is possible to see that above critical frequency, radiation power tends to be asymptotic around the value of $\frac{k}{k_B} = 1$ for each mode rather than below where values of radiation efficiency largely differ one from another, also between odd and even of the same mode [7]. Thus for the finite dimension plate radiation efficiency below the critical frequency may not be neglected as the infinite panel suggests. Furthermore most of the propagated radiation is made by the residual half-cell pairs remaining at the edge of the panel. As mentioned before, the panel can be though as an array of monopole-source due to the phase shift occurring between two adjoining point sources, sound power flow is limited. So the half-cell remaining at the corner are responsible of the sound radiated. More configurations, depending on the mode shape, are possible.

Therefore right now only a single coupled mode was considered to calculate the radiation efficiency, thus it cannot be directly applied in practical

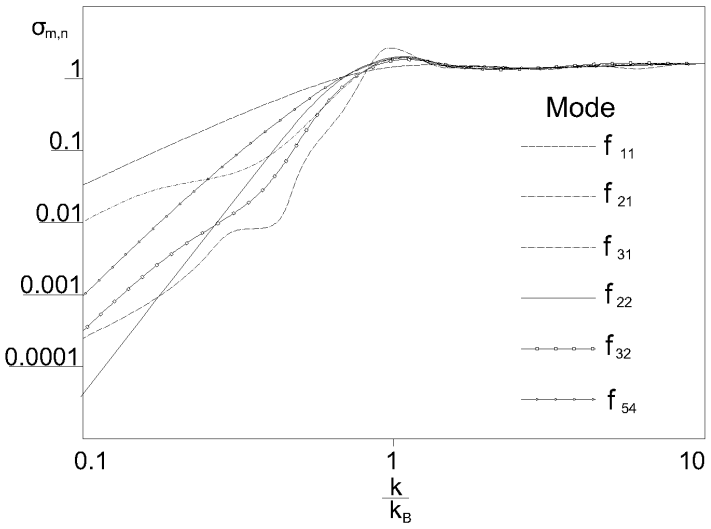

Figure 2.12: Modal Radiation efficiency

situations because the plate involve a combination of modes. The radiation efficiency then is defined as the weighted average of the single modes:

$$\sigma = \frac{\sum \sigma_n v_n}{\sum v_n^2} \tag{2.80}$$

It must be noted that light damped material are assumed, thus modal analysis is studied as a solution of eigenvalues, however this is not truly correct because damping can not be sometimes be express through the Rayleigh damping model [1]. Moreover the concept of a frequency-average radiation efficiency based upon the space-average mean square vibration velocity is not tenable in the case of highly non uniform structures or/and highly damped structures due to non-uniform distribution of mode.

Radiation efficiency of orthotropic finite plates

For an orthotropic vibrating plate, the general equation motion of the element is known represented by the Eq. (2.30) as the section largely discuss it. From modal analysis the structural wavenumber must equal the Eq.n (2.40) in order to solve the motion equation.

$$k_{m,n} = k_B \tag{2.81}$$

where $k_{m,n} = [k_m k_n] = [\frac{m\pi}{L_x}, \frac{n\pi}{L_y}]$ then, as already shown in equation (2.41), frequency of resonant modes can be found.
In order to evaluate the radiation efficiency of orthotropic plate an additional hypothesis needs to be made [5]:

1. in a narrow frequency band the discrete distribution of modes can be treated as continuous
2. resonant modes are responsible of sound radiation
3. the modes are linearly independent
4. the vibrational energies of the resonant modes in a narrow frequency band have equal value (equipartition of modal energy).

Thus the average radiation efficiency of resonant modes within frequency band $\Delta\omega$ is defined as:

$$\bar{\sigma}(\omega_0, \Delta\omega) = \frac{\int_{\omega_0}^{\omega_0+\Delta\omega_0} \int_0^{\frac{\pi}{2}} \sigma(\omega,\theta) k_B \frac{\partial k_B}{\partial \omega} d\theta d\omega}{\int_{\omega_0}^{\omega_0+\Delta\omega_0} \int_0^{\frac{\pi}{2}} k_B \frac{\partial k_B}{\partial \omega} d\theta d\omega} \tag{2.82}$$

by knowing the number of modes in an orthotropic plate within$\Delta\omega$ frequency band:

$$N(\Delta\omega) = \frac{L_x L_y}{2\pi^2} \sqrt{\rho h} \Delta\omega \int_0^{\frac{\pi}{2}} \sqrt{\frac{1}{D(\theta)}} d\theta \tag{2.83}$$

It must be noted that the above equation need to be considered in an elliptical distribution of k_B. Hence the modal density $\frac{\partial N(\omega)}{\partial \omega}$ is:

$$n_d = \frac{L_x L_y}{2\pi^2} \sqrt{\rho h} \frac{F(\frac{\pi}{2}, r)}{\sqrt[4]{D_x D_y}} \tag{2.84}$$

where $F(\frac{\pi}{2}, r)$ is the complete elliptic integral of the first kind, defined as:

$$F\left(\frac{\pi}{2}, r\right) = \int_0^{\frac{\pi}{2}} \sqrt{\frac{1}{1 - r^2 \sin^2 \gamma}} \tag{2.85}$$

then the equation(2.81) can be rewritten as:

$$\bar{\sigma}(\omega_0, \Delta\omega) = \frac{l_x L_y}{\pi^2} \frac{\int_{\omega_0}^{\omega_0+\Delta\omega_0} \int_0^{\frac{\pi}{2}} \sigma(\omega,\theta) k_B \frac{\partial k_B}{\partial \omega} d\theta d\omega}{N(\Delta\omega)} \tag{2.86}$$

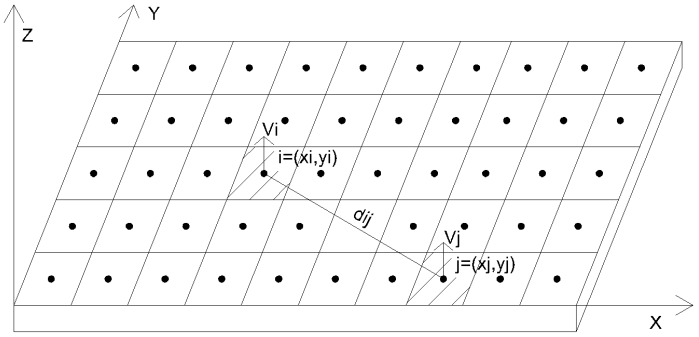

Figure 2.13: Subdivided panel into elementary radiators

Therefore to calculate the radiation efficiency must be know the relation that exists between the wave number and frequency, or the relation ship between the phase velocity against frequency also knows as *Dispersion curve*. Next chapter will introduce some of the algorithm that can be used to estimate the image dispersion of a plate processing the signal recorded by accelerometers.

2.5 Discrete Calculation Method

Discrete Calculation Method (DCM) is a non modal approach to evaluate the sound radiation efficiency from experimental vibrations velocity [6]. The idea is to evaluate the radiated power of the whole plate as a sum of piston radiators in which the plate is subdivided. Thus the surface of the plate is virtually subdivided into a grid of N-rectangular elements, in which the transverse vibration field of each radiators is known (Fig. 2.13).

The overall vibration of the panel can be described by the column of complex vector of velocity amplitude:

$$\bar{v}_e = \begin{bmatrix} v_{e1} & v_{e2} & \cdots & v_{eN} \end{bmatrix}^T \tag{2.87}$$

Each individual element is tread as a circular piston in order to obtain the

sound power radiation from the radiation impedance of circular piston vibrating plate. In fact assuming that the dimensions of the elements are small compared to both structural and acoustic wavelengths, the total radiated power can be expressed as:

$$\bar{P}(\omega) = \sum_{k=1}^{N} \frac{1}{2} a_i Re(\bar{v}_e \bar{p}_e) \tag{2.88}$$

then from the integral formulation of Rayleigh [4] it can be derived:

$$\bar{p}_{ei}(x_i, y_i) = \frac{j\omega\rho_0 a_i e^{-jkd_{ij}}}{2\pi d_{ij}} \bar{v}_{ej}(x_j, y_j) \tag{2.90}$$

$$\left[\bar{p}_e\right] = \left[\bar{Z}\right]\left[\bar{v}_e\right] \tag{2.91}$$

where $[\bar{Z}]$ is the matrix incorporating the point and transfer acoustic impedance terms over the grid of elements. This terms of impedance can be subdivided into self radiation impedance z_{ii} and mutual radiation impedance z_{ij}. The self radiation impedance of i-th element is:

$$z_{ii} = \rho_0 c s_i \left[1 - \frac{J_1(2ks_i)}{ka_i} + i\frac{S_1(2ks_i)}{ks_i}\right] \tag{2.92}$$

where ρ is the air density, c sound velocity into the fluid, s_i is the equivalent radius of the i-th elements, k is the wavenumber of sound, J_1 is the first order Bessel function, S_1 is the Struve function and i the imaginary unit.
The mutual radiation impedance z_{ij} of the i-th element for the sound pressure produced by the vibrational velocity of the j-th element can be approximated as:

$$z_{ij} = \frac{\rho_0 c k^2 s_i s_j}{2\pi}\left[2\frac{J_1(2ks_i)}{ka_i}\right]\left[2\frac{J_1(2ks_j)}{ka_j}\right]\left(\frac{\sin kd}{kd} + \frac{\cos kd}{kd}\right) \tag{2.93}$$

Thus the radiated sound power is :

$$W_i = Re(z_{ii})|v_{ii}|^2 + \sum_j Re\left(z_{ij} v_i v_j^*\right) \tag{2.94}$$

[4]

$$p(\bar{r}, t) = \frac{j\omega\rho_0}{2\pi} e^{j\omega t} \int_S \frac{v_n(\bar{r}_i) e^{-jkR}}{R} dS \tag{2.89}$$

where v_n is the complex normal velocity amplitude of the i-vibrating piston

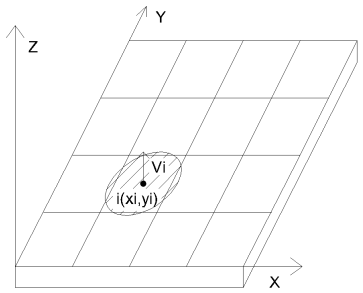

Figure 2.14: Single vibrating piston

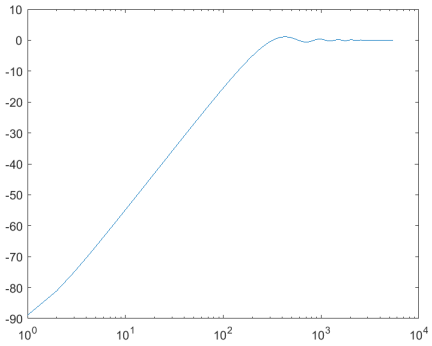

Figure 2.15: Radiation efficiency of a single piston

where v_j^* is the conjugate complex velocity of the j-th elements.
Sound radiation efficiency can be obtained by normalizing the result of Eq.(2.94) with the hypothetical sound power radiated from a piston having the dimension of the whole surface plate vibrating with the mean square velocity of the measured point.

$$\sigma = \frac{\sum W_i}{\rho_0 c \langle v^2 \rangle S} \tag{2.95}$$

The DCM method was implemented using MATLAB software©in order to analyze sound radiation of CLT panel.
Consider for a moment that in the panel just one accelerometer is vibrating as Fig. 2.14 shows. It means that only one circular piston is working, thus it will be expected to visualize a theoretical behavior of the radiation power similar to Fig. 2.12

Applying DCM transformation to single vibrating piston at frequency of 400 Hz, the result is shown in Fig. A.2

Comparing the result with a single mode radiation efficiency shown in

Fig. 2.12, it can be found that the MATLAB code is correctly written.

2.6 CSTB method

CSTB method was proposed by Villot and Guigou-Carter [8] to evaluate the radiation efficiency for lightweight elements. This method requires both structural and air pressure measurement fields. Thus radiation efficiency can be evaluated as:

$$10\log_{10}(\sigma) = L_p - 6 - L_v + 10\log_{10}(\frac{A}{S}) \tag{2.96}$$

where L_p is the spatially average sound level radiated in the receiving room, L_v is the spatially average level of the element tested and A the equivalent absorption area of the receiving room [9]. While L_p is directly measured by the sound-level meters. The measurement were carried out using tapping machine as a mechanical source, white noise and sine sweep as air-borne excitation. However using electromagnetic shaker to evaluate radiation efficiency can be problematic since a using of point source generates a bending wave near field. Radiated power from bending near field wave is equal to the radiate power of the element if this has infinite extent dimension while resonant field radiated power is the power which is radiated from the finite elements due to the reflections from the edges. This two forms of radiation are very close at and above the critical frequency thus is difficult to distinguish one from the other. A ratio e between resonant radiated sound power and the bending wave near field radiated sound power below critical frequency is calculated as:

$$e = \frac{P_r}{P_n} = \frac{\pi f_c \sigma_r}{4 f \eta} \tag{2.97}$$

since only the resonant radiated power is needed, the following correction has to be applied :

$$P_r = \frac{1}{1 + \frac{1}{e}} \tag{2.98}$$

Chapter 3

Determination of the wavenumber

Acoustical signals may be processed to obtain empirical data from the measurements. This chapter provide a comparison between the methods in order to identify the ones which are better suited ti the purpose of this work. In order to evaluate the dispersion curve of the vibrating plates, the velocity of the bending waves which propagate in the solid must be estimated. So, knowing the distance between the receivers, finding out the time of flight (ToF), phase velocity can be estimated:

$$v_\phi = \frac{\Delta x}{t} \tag{3.1}$$

where Δx is the space between the receiver, and t is the time of flight evaluate. Four algorithms are taken from the literature known as: *Maximum peak* [10], *Minimum Energy* [11], *Kurtosis cumulative sum*[12], *Phase shift velocity* [13] compared to *Tau-p Transformation* [14].

3.1 Time of flight

The analysis of sound signals using the time of flight method is possible in a specific frequency range. In fact the range of application of ToF is related to the distance between the receivers, for low frequencies having wavelength bigger than the distance between the accelerometers this approach cannot be taken into account. Thus for low frequencies the dispersion curve is calculated with the phase difference between two subsequently signal. The frequency limit, which devise phase and ToF approach, cannot be calculated previously because the phase velocity is unknown. Thus both methods will be applied for a bigger range in order to overlap the two methods around the guessed limit frequency.

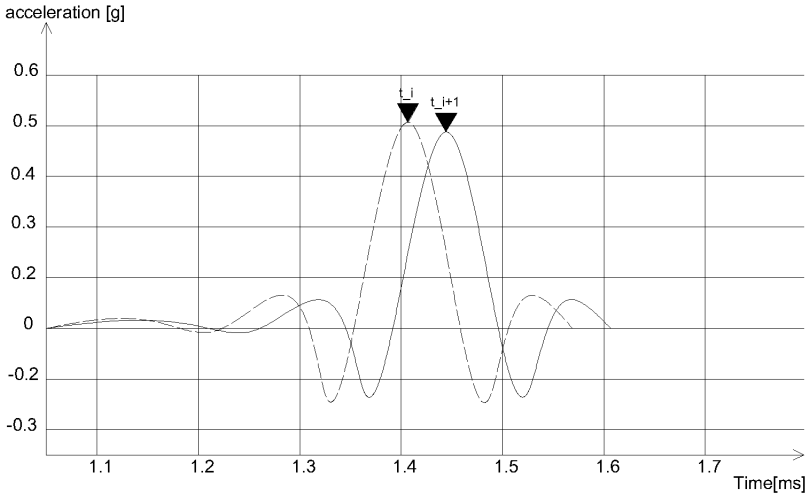

Figure 3.1: Wave velocity determined by using maximum peak method

3.1.1 Maximum peak

The maximum peak algorithm is based on the idea that the onset signal is defined by the absolute maximum of the reached signal [10]. For example if we consider a pulse centered on a known frequency, the time signal recorded by the second accelerometer will be attenuated and time delayed from the first one. Choosing the absolute maximum, ToF can be easily estimated:

In this way all the velocities related to the pulse frequency center can be obtained, and the dispersion curve of the element can be built. Other applications of this method prefer to use the first relative maximum that occur sooner than the other one, no scientific reason demonstrate that choosing absolute maximum rather than first relative maximum, have better resolution.

3.1.2 Minimum energy

The minimum energy algorithm is based on the idea to estimate the onset signal since the energy suddenly increases at the front waves [15]. The formulation of the computation lies on the theory of the cumulative summation, in which step by step the energy increases: normal cumulative sum, in a pulse, is constant (or slightly sloped) and increases rapidly when the maximum of

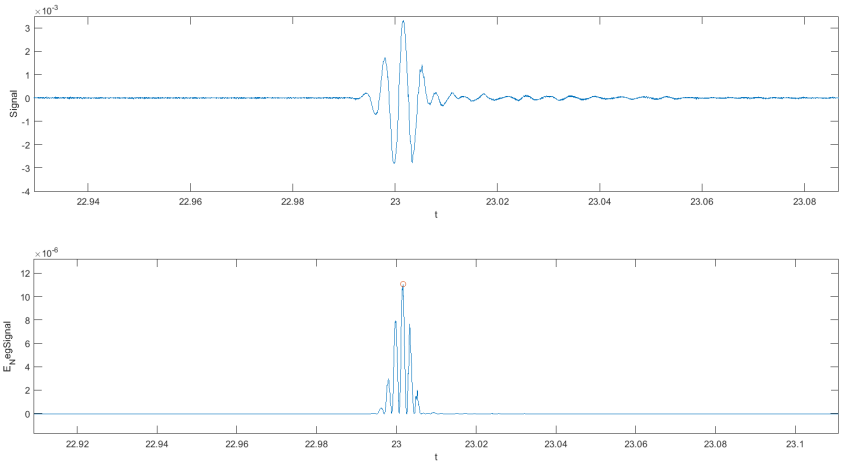

Figure 3.2: 100Hz pulse top and minimum criteria energy bottom

the signal is reached.

$$E_c(n) = \sum_{m=1}^{n} s^2(m) \tag{3.2}$$

Looking at Eq. (3.3), a negative slope is added to the formulation of cumulative sum, thus instead of step increasing of the energy summation the result will have a negative slope and will reach a relative minimum when the maximum of the onset signal occurs.

$$E_{neg}(n) = E_c(n) - an\frac{E_N}{N} = \sum_{m=1}^{n}\left(s^2(m) - an\frac{E_N}{N}\right) \tag{3.3}$$

where N is the signal length, E_N is the total energy, a is the slope (normally is set to one). Figure 3.3 shows an example of five pulses at 100 Hz:

It should be noted that in this case, the function E_N *signal* is the minimum criteria energy de-trended to guarantee a better peak choosing algorithm. Therefore this algorithm changes a little bit the approach: from finding the minimum peak into finding, again, the absolute maximum: this can be though as a choosing parameter a (slope) in order to flatten the decrease. Replacing the computation for the subsequent accelerometers (spaced by Δx m) the time of flight can be estimated.

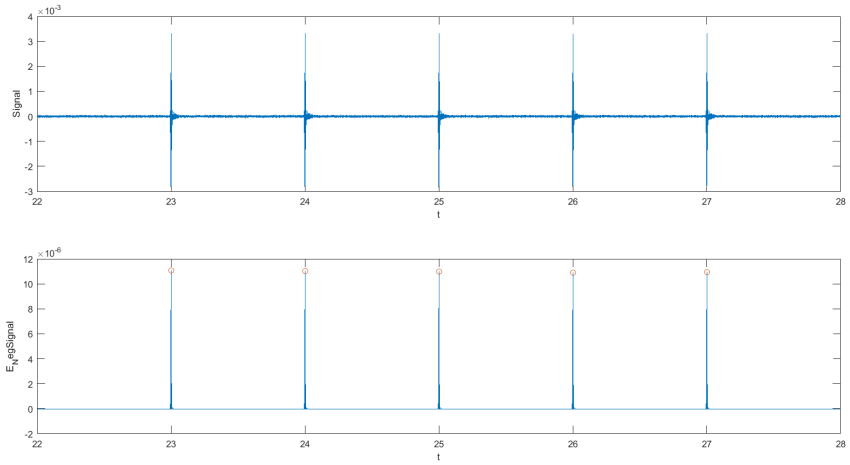

Figure 3.3: Applying minimum criteria energy to a train of pulses

3.1.3 Kurtosis Criteria

Kurtosis statistic parameter is defined as the ratio between the fourth and the second moment of the set of data, and it describes the shape of a probability distribution. When withe noise occur the data distribution have Gaussian shape and the value are close to the average thus kurtosis take a steady value. While when the on set signal occur the high amplitude value would extend the tail of the distribution and kurtosis will reach rapidly change in value. Thus on-set signal is defined where the kurtosis takes increase suddenly. The cumulative kurtosis of the signal $s(t)$ can be calculated by:

$$k(n) = \frac{\frac{1}{n}\sum_{m=1}^{N}\left[s(m) - \bar{s}\right]^4}{\frac{1}{n}\sum_{m=1}^{N}\left[s(m) - \bar{s}\right]^2} \tag{3.4}$$

where $\bar{s}$ denotes the mean of $s(t)$, n is the variable of the signal length. To better find the maximum peak of the kurtosis in which onset signal is represented, an analog to minimum energy code manipulation can be made:

$$k_{neg(n)} = \sum_{m=1}^{n} k(m) - n\frac{\sum_{m=1}^{N} k(m)}{N} \tag{3.5}$$

Thus taken the corresponding time of direct path, the phase velocity can be evaluated.

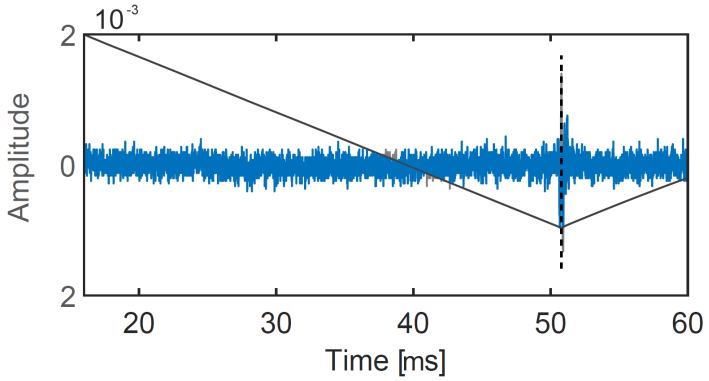

Figure 3.4: Kurtosis parameter

3.2 Dispersion curve

Until now the algorithm shown taken into account a single couple of signals one at time, thus can be calculated the ToF by knowing the distance between two accelerometers, sometimes measurement are made with more than two receiver thus can be convenient use a multi-channel analysis of sound waves in order to directly gather the dispersion curve without calculate each single time delay between receiver.

3.2.1 The Radon Transform

Introduced by Radon in 1917, the transformation known as "$\tau - p$" or "Radon transform" was originally formulated as an integration of a 2D function along a line expressed in polar coordinates $\mathrm{l}(\rho; \theta)$. The first significative application of the Radon transform is the reconstruction of a bi-dimensional image from stack data of computed axis tomography scans. More recently it has been applied, in a generalized form, in the contest of seismology[16]. Thus the image dispersion of a layered medium can be reconstructed by applying two linear transformations: the Radon transform and Fourier transform, to the recorded wave field.

In seismology, once measured the propagation signal with a geophone, a slant stack operator is first applied to the gather recorded linearly transform wave field. Let consider $u(x,t)$ represent the seismic signal, where x is the space domain variable and t the time domain variable. For a continuous signal the slant stack is defined as:

$$u(p,\tau) = \int u(x, t = \tau + xp)dx \tag{3.6}$$

where p denotes the "slowness" (is the inverse of velocity) or "ray parameter", and τ denotes the intercept in the time domain.
This can be seen as a sum of the values along a line defined by a slope for each intercept time value:

$$t = px + \tau$$

If we apply the Fourier transform to Eq. (3.6), we get:

$$U(\omega p, \omega) = \int u(p, \tau) e^{i\omega\tau} d\tau \tag{3.7}$$

This is equal to the application of 2D Fourier transform to the gather recorded:

$$U(k, \omega) = \iint u(x, t) e^{i\omega t - ikx}\, dx\, dt$$

recalling the ray parameter $p = \frac{k}{\omega}$:

$$U(\omega p, \omega) = \iint u(x, t) e^{i\omega(t - px)}\, dx\, dt$$

Using the variable $\tau = t - px$, and adjusting the integral:

$$U(\omega p, \omega) = \int e^{i\omega(t-px)} \left(\int u(x, \tau + px)\, dx \right) dt$$

Note that the integral in brackets is exactly equal to eq. (3.6).

Let consider an example of gather recorded, shown in Fig. 3.3. On the left side it is shown a continuous signal recorded by 5 geophones; let consider "δ "as the geophone number identification. The summed amplitude along a slope, can be easily recognized; in fact if we display the value of the amplitude as a scale of colors, going from black (biggest) to white (lowest), we can represent it in a diagram with $\tau - p$ axes. In this case, considering the same intercept time τ, changing the slope the summed value change. As displayed on the right side of Fig. 3.3, for the same "τ" three different values

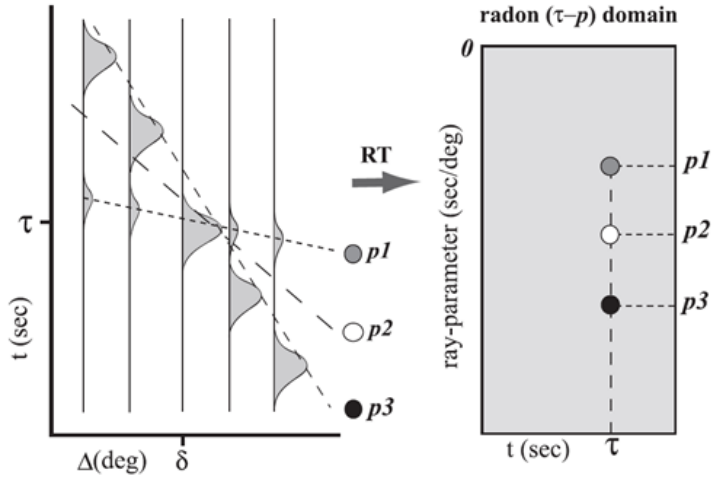

Figure 3.5: Left side: recorded signal. Right side: $\tau - p$ diagram: the colored points represent the value of the summed amplitude, from black (biggest) to white (lowest)

appears: the slope "p_3" corresponds to the maximum value due to the fact that with this angle the dashed line intercepts all maxima of the amplitude of the signals; on the other hand "p_2" does not intercept any other value and thus corresponds to the minimum value. Thus this method, called also "pattern recognition", can find out which are the relative amplitude maxima, with references to the slope (velocity), and therefore which are the velocities that gives the highest displacement (mode).

3.2.2 The Phase-Shift method

Introduced by C.B. Park, R.D. Miller and J. Xia [17], the phase-shift method provides image dispersion curves of different modes with a high-resolution. The idea of the transform comes from the fact that when two or more waves are summed with the same phase, then the amplitude will reach a maximum, while on the contrary out-of-phase waves give a de-constructed reflection. Therefore, choosing a right velocity to shift the phase of the signals, a summed amplitude will have a maximum; moreover if the track are normalized the maxima will have the value of one. For a better explanation let consider $u(x,t)$ a gather of signals recorded by N geophones, where x represents the space domain variable and t the time domain variable. Let's call u_i the i-track recorded by the i-geophone with $i = (1, 2, ...N)$[5].

With reference to Fig. 3.4, consider, as a simplified case, that the signal recorded by the geophone is a sinusoid; therefore, when the slope (velocity)

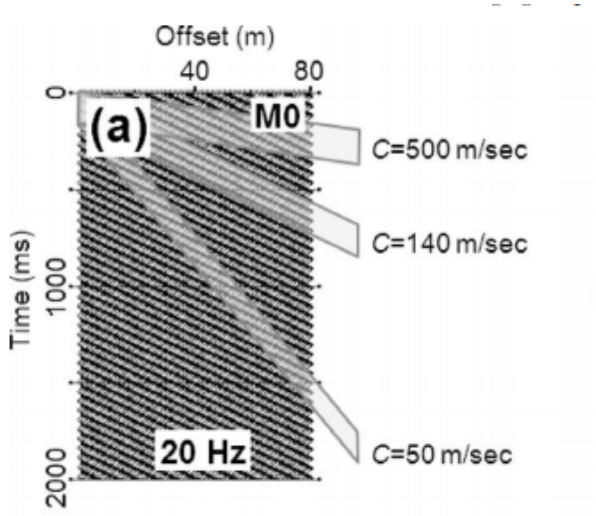

Figure 3.6: Signal recorded by the accelerometers

intercepts the the same phase, the summed amplitude reaches a maximum, otherwise it will be lower.
If the FFT (Fast Fourier transform) is applied to the traces:

$$U_i(\omega) = FFT(u_i) \tag{3.8}$$

or, for a continuous signal:

$$U(x,\omega) = \int u(x,t)e^{i\omega t}dt \tag{3.9}$$

Then $U(x,\omega)$, eq. 3.9, can be expressed, as a complex number, having amplitude (A) and phase(P):

$$U(x,\omega) = A(x,\omega)P(x,\omega) \tag{3.10}$$

The phase term can be expressed as:

$$P(x,\omega) = e^{-i\Phi x} \tag{3.11}$$

so that:

$$U(x,\omega) = A(x,\omega)e^{-i\Phi x} \tag{3.12}$$

where $\Phi = \frac{\omega}{c_\omega}$ and ω is the frequencies in radians. The phase contains the information about the dispersion properties, while the amplitude contains

all the other properties(spherical divergence, attenuation) [13]. Therefore U(x,ω) can be normalized by the amplitude:

$$U_N(x,\omega) = \frac{U(x,\omega)}{|U(x,\omega)|} = \frac{A(x,\omega)}{|A(x,\omega)|}P(x,\omega) \tag{3.13}$$

Applying the following integral transform to eq. (3.9):

$$V(x,\phi) = \int e^{i\phi x}\frac{U(x,\omega)}{|U(x,\omega)|}dx = \int e^{-i(\Phi-\phi)x}\frac{A(x,\omega)}{|A(x,\omega)|}dx \tag{3.14}$$

Eq. (3.9) can be thought of as the sum over a set of wave fields, which are function of frequency, after applying an offset-dependent phase shift determined for an assumed phase velocity $c_\omega = \frac{\omega}{\phi}$ to the wave field. Therefore, when the $\phi = \Phi$, the integral will reach the maximum of the amplitude:

$$\phi = \Phi = \frac{\omega}{c_\omega} \tag{3.15}$$

Dispersion curves can be found extracting the peak of the image dispersion $V(x, c_\omega)$ by changing the variable c_ω, for a given ω.
A synthetic example can be seen in Appendice A (Fig. B.6 Fig. B.6), on the pictures show the image dispersion of a wave centered in one frequency having two different propagation velocity, so that two points at same frequency can be noted.

3.2.3 Inhomogeneous wave correlation

This method a provide propagation constant for two-dimensional structures, such as plate. Knowing that propagation is time and spatially depending the Inhomogeneous Wave Correlation takes into account a double Discrete Fourier Transform (DFT) transformation of the signals, thus the spatial domain is transformed into wavenumbers domain (k-space) and the time domain is converted into frequency domain (f-domain).

$$FFT[s(t,x)] = s(f,x) \qquad \mapsto \qquad FFT[s(f,x)] = s(f,k) \tag{3.16}$$

Thus this transformation is also known as f-k transform. Recently upgrade, found that using IWC internal loss factor can be evaluated from the imaginary part of the wavenumbers. In this section we are mainly interested into the real part of the wavenumber thus image dispersion can be shown. However the theory of the IWC method is briefly introducted after [18].

First we assume a harmonic field either from harmonic excitation or from a temporal Fourier transform:

$$w(x,y,t) = \int_0^\infty \widehat{w}(x,y)e^{i\omega t}d\omega \tag{3.17}$$

where the hat $\widehat{w}$ define the ω-dependence of the signals. Then the Inhomogeneus wave is defined as:

$$\widehat{o}_{k,\gamma,\theta}(x,y) = e^{-ik(\theta)(1+i\gamma(\theta))(x\cos(\theta)+y\sin(\theta))} \tag{3.18}$$

where $\widehat{o}_{k,\gamma,\theta}(x,y)$ is a wave with heading θ, attenuation γ, and apparent wavelength $\lambda_a = \frac{2\pi}{k}$. Then the correlation between the inhomogeneous wave and the complete wave field is calculated as:

$$IWC(k,\gamma,\theta) = \frac{|\int\int_S \widehat{w}\widehat{o}^*_{k,\gamma,\theta}dxdy|}{\sqrt{\int\int_S |\widehat{w}|^2dxdy}\int\int_S |\widehat{o}_{k,\gamma,\theta}|^2dxdy} \tag{3.19}$$

the symbol $*$ denotes the complex conjugate. We assume that wave field $\widehat{w}$ is known on arbitrary data point (x_i, y_i). It should be noted that the input field can be either experimental or numerical.

Chapter 4

Experimental evaluation of radiated sound power

This chapter describes the measurements carried out in the laboratory. The goal is to evaluate the radiation efficiency of a rectangular cross laminated timber (CLT) plate by using different kinds of sources: a shaker and a loudspeaker. The main problem of CLT structures is the poor sound insulation performance due to the relative high stiffness combined with a relative low density. Although many papers present experimental and numerical methods to evaluate radiation efficiency, there are no standard procedures to measure the acoustic parameter. The radiated sound power will be evaluated for a CLT plate having simply supported edges on two sides and free edges on the other two. The geometric characteristics of the plate are shown in Fig. A.3. The floor installed in the acoustic transmission chambers is made by 4 CLT panels, fixed with couple of screws with an angle of 45°. To evaluate the radiation efficiency, two formulations are taken in to account: the method developed by CSTB and the Discrete Calculation Method (DCM).

4.1 Measurements set up

The measurements were carried out in the acoustic laboratory the Department of Industrial Engineering of the University of Bologna. The plate was tested in a facility having two rooms separated by the CLT elements. The source room has a volume of 36 m^3 and receiving room has a volume of 56 m^3. Two main kind of measurements were carried out: a first one using both mechanical and airborne sound excitation with microphones as a receivers, and a second one using, again, the same mechanical and airborne excitation but recording the output with accelerometers. Fig. A.2 shows a conceptual

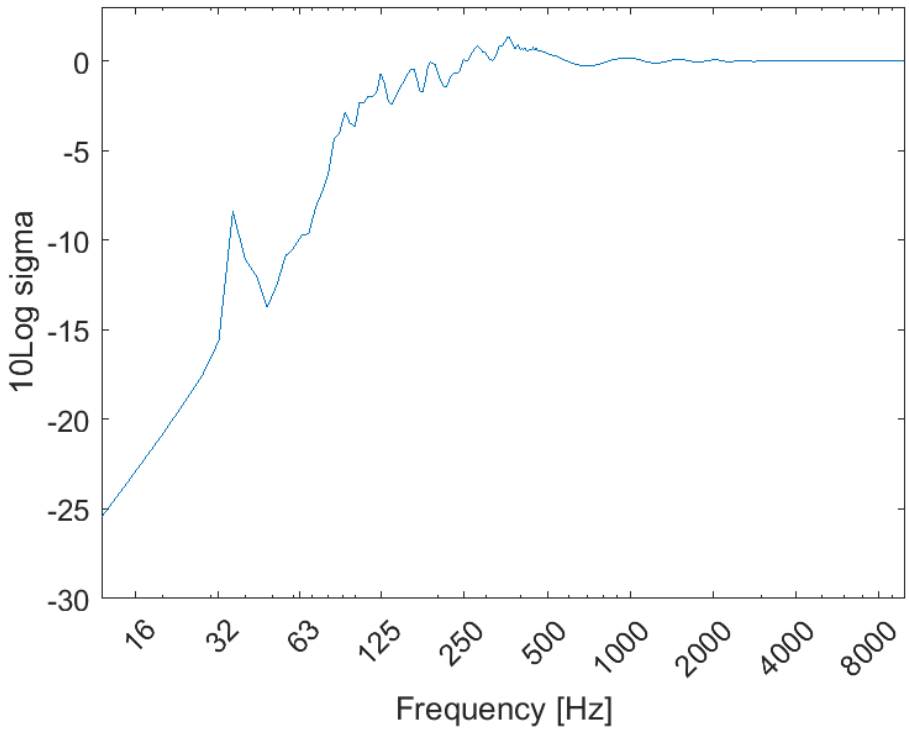

Figure 4.1: DCM method: radiation efficiency using sine sweep

scheme of measurement chain.

4.2 Measurements: DCM method

DCM measurements take into account a structural excitation with two input signals: white noise and exponential sine sweep. Both sound signals cover the range of frequency from 30 Hz to 8000 Hz. The source and the accelerometers were positioned in the same side of the CLT plate. A grid of 150 receivers was installed and three accelerometers were used at a time, therefore measurements were repeated many times until all of the receiving points were evaluated. In order to ensure the reproducibility of the measurements, a shaker was used as a mechanical excitation source in order to have the same loading force. The position of the source and receiver can be seen in Fig. A.3
The DCM algorithm was implemented using MATLAB program in order to evaluate the plate radiation efficiency.

Analyzing the CLT plate with the DCM method, shown in Fig. 4.1 and

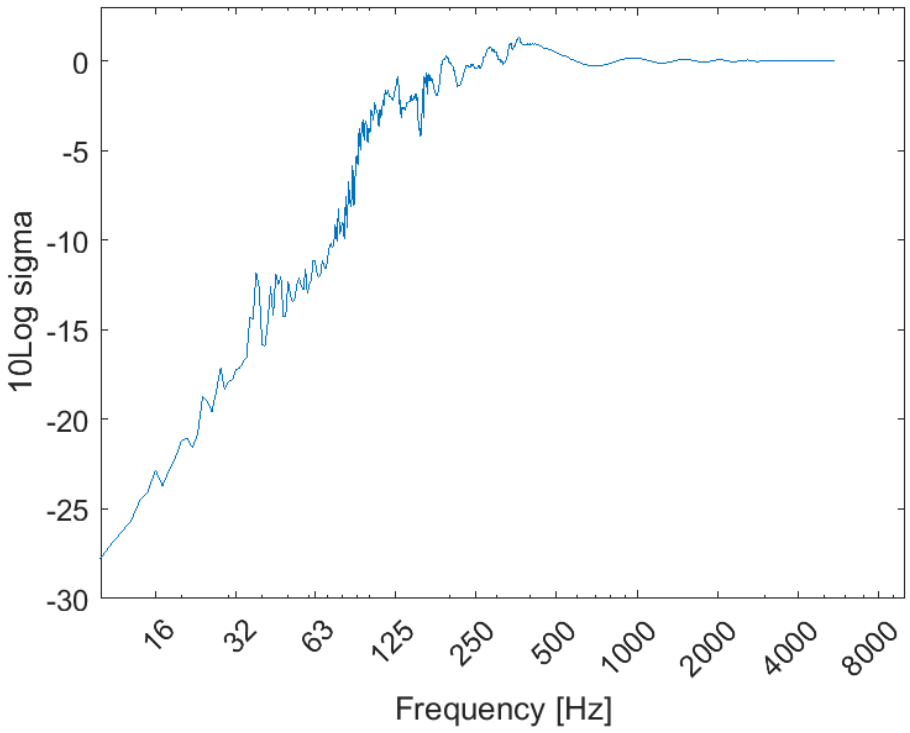

Figure 4.2: DCM method: radiation efficiency using white noise

Fig. 4.2 it is possible to see that radiation efficiency calculated reaches the maximum at the frequency of 440 Hz. After this frequency the value of the power radiated tends asymptotically to zero, and this confirms that 440 Hz is the critical frequency. In fact, as explained in section 2.4, critical frequency is defined as the first coincidence frequency in which both acoustic and structural wave number are equal thus the radiated sound power reaches the highest value. Before this frequency limit, the regime of sound propagation can be described as modal summation due to low mode density and it results that the plate is a bad radiator.
With both input sources it can be seen that in the frequencies around 40 Hz the radiation efficiency has a relative maximum. The peak reaches a higher value when sine sweep is used: probably the input signal excited the plate better, therefore the modal radiation is higher than when white noise is used as input signal. Anyhow the peak appears in both result of radiation efficiency. Studying the modal vibration of the plate, first mode can be observed at the frequency of 40 Hz Fig. 5.3, thus the radiation efficiency spot at 40 Hz can be associated to the first mode.

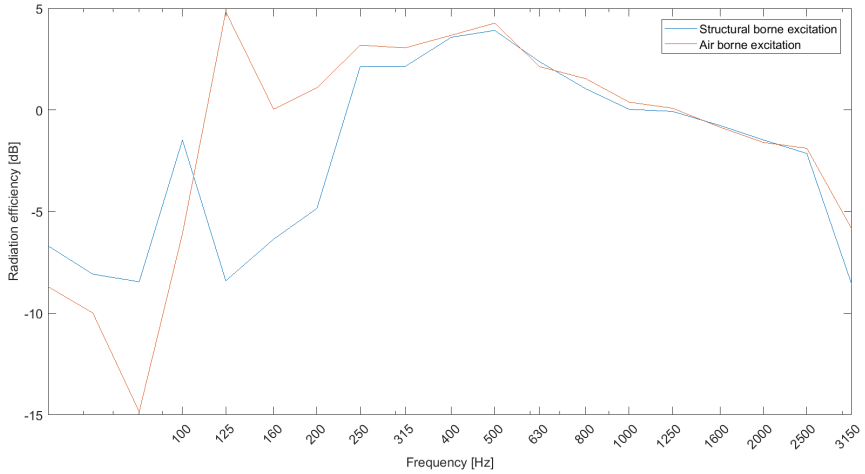

Figure 4.3: CSTB method: radiation efficiency

4.3 Measurements: CSTB method

According to the CSTB method, the vibration velocity of the plate and the sound pressure level in the receiving room were measured at the same time. In this case the source and the receiving elements were not located in the same room. Two kind of source excitation were used, mechanical - tapping machine - and air borne excitation - loudspeaker-. Thus two curves of sound radiation are found. Signal input for loudspeaker was the same used for the shaker i.e. white noise and exponential sine sweep, so the same aforementioned observations are valid. Fig. A.2 (a) shows the location of loudspeaker while Fig. A.2 (b) shows the position (in the source room) of the tapping machine. As aforementioned in section 2.6 velocity level vibration of the plate and sound pressure field in the receiving room were measured at same time for each source type. Thus two radiation efficiencies can be evaluated with Eq. (2.96): using airborne and structure-borne excitation. Fig. A.8 shows the accelerometers and sound-level meters position. The accelerometers were installed in the panel using magnets.The result of CSTB evaluation can be seen in Fig. 4.3. CSTB approach results show a match with the results obtained by DCM approach. At the frequency of 400-500 Hz the airborne and structure-borne radiation efficiency match perfectly and for higher frequencies both curve does not much differ. Thus the critical frequency can easily seen: both sound radiation reach the same maximum value at the same frequency. Moreover below the 440 Hz the panel radiates sound power badly: for frequencies lower than critical one, modal regime occurs and the sound radiated from the edge. For frequencies higher than 2500 Hz radia-

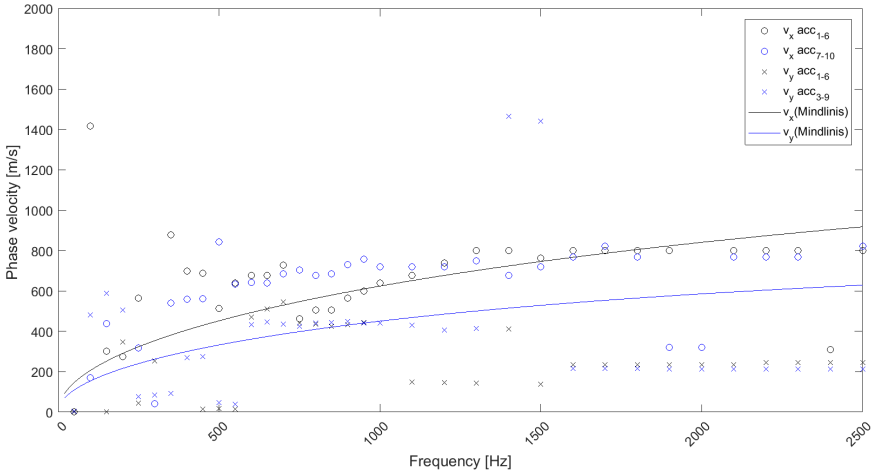

Figure 4.4: Maximum Peak Method - Dispersion curve

tion efficiencies from structural and airborne excitation start to differ. This might be determined by the characteristics of the testing facilities, then these values should not be taken into account. At 125 Hz with airborne excitation a peak appears in the estimation of the radiation efficiency; this dip in sound reduction index has been spot in other measurements dealing with the characterisation of CLT elements and therefore could be connected to the characteristics of the slab itself.

4.4 ToF Algorithms

To evaluate the dispersion curve by Time of Flight algorithms shows in chapter 3.1 the measurement set up displayed Fig. A.4 was mounted. The idea is to evaluate how the signal spreads among the two main directions of the solid by using a multi-channel analysis. The exciting source used was a shaker and the signal input was a train of 5 pulses centered at specifics frequencies. The frequencies investigated ranged from 50 Hz to 1000 Hz with a step of 50 Hz and from 1000 Hz to 4000 Hz with a step of 100 Hz. Thus for each frequency, the time of flight and the relative wavenumber can be calculated. Knowing the frequency dependance of the structural and acoustical wavenumbers and knowing the dispersion curve is possible to estimate the critical frequency and the coincidence frequency of plate. The algorithms were implemented with the MATLAB software. Results will be compared with theoretical curve evaluate with the equation (2.23), using the property value found in the schedule of the material, shown in table one. The phase

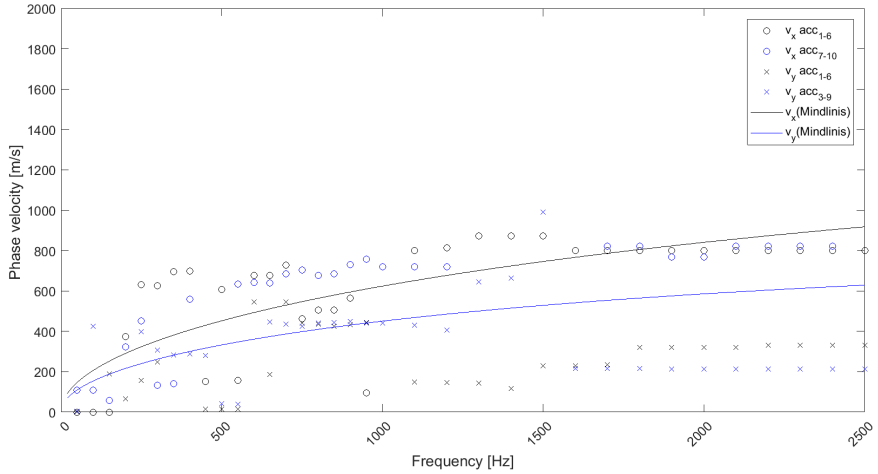

Figure 4.5: Minimum Energy Method - Dispersion curve

velocity is calculated analyzing four different couples of accelerometers: two couples in the x-axis (positions 1-6 and 7-10) and other two couples in the y-axis (positions 1-6 and 3-9).

E_x	E_y	ν_{xy}	ν_{yx}	h
12000000 kN/m^2	400000 kN/m^2	0.97	0.093	0.16 cm

4.4.1 Maximum peak algorithm

Fig.4.4 shows the result the Maximum peak algorithm applied to the x-axis. The axis of frequency is cut at 2500 Hz due to the resolution of the sample frequency. In x-direction the phase velocity tends to the value of 800 m/s while the frequencies increase. This result shows a good agreement with the theoretical Mindlin's dispersion curve. For frequency lower than 500 Hz the result start to display a greater statistical deviation. The results on y-axis in the range above 1500 Hz shows a deviation from the theoretical dispersion curve calculated with Mindlin's relation Eq. (2.44). The values for the rest of the frequency range match quite well and gives correct values of phase velocity. The coincidence frequency can be seen calculating the structural wavenumber and comparing it with the acoustic wavenumber, Fig. 5.6 and 5.7 shows the results.

4.4.2 Minimum energy algorithm

Fig.5.2 (c) shown the result of applying, in the x-axis, the Minimum energy algorithm. The phase velocity is calculated analyzing four different couples of

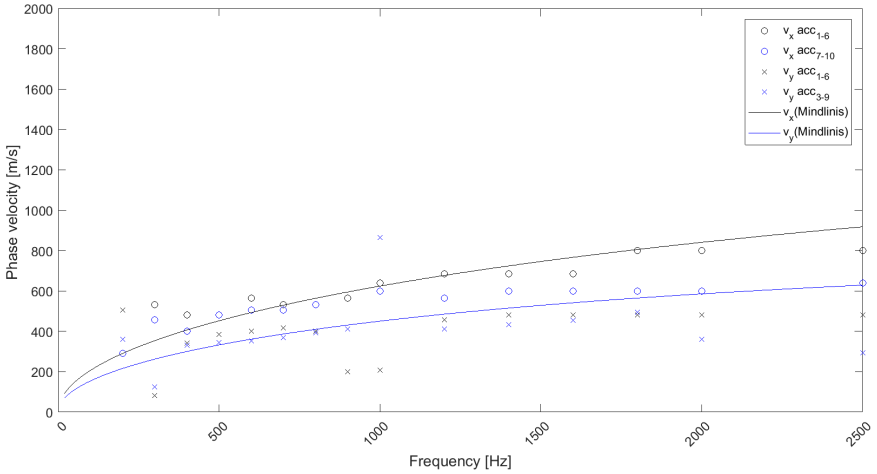

Figure 4.6: Kurtosis Method - Dispersion curve

accelerometers: two couples in the x-axis (positions 1-6 and 7-10) and other 2 couples in the y-axis (positions 1-6 and 3-9). In the x-direction the phase velocity tends to the value of 800 m/s while the frequencies increase, showing also in this case a good agreement with the theoretical Mindlin's dispersion curve. For frequencies lower than 500 Hz the results start to differ from the theoretical curve. On the y-axis the result appears to have greater dispersion: for frequencies grater than 1500 Hz the reached value is about 300 m/s, while the theoretical Mindlin's dispersion curve assumes grater values. Moreover the phase velocity values calculated analyzing two different couple (positions 1-6 and 3-9) of receiver slightly differ from each other. Comparing this result with the value finding out using the Maximum peak the result match. This does not guarantees that dispersion curve is correct. It rather means that the two algorithms find mostly the same on-set part of the signal. This is quite obviously because the amplitude peak is related with energy peak, thus this two method are connected. Even if these methods work almost in the same way, a smoother result is found with energy minimum while the Maximum algorithm sometime gives overload peaks.

4.4.3 Kurtosis algorithm

Fig.4.6 shows the result of the application of the Kurtosis energy algorithm in the x-axis. The phase velocity is calculated analyzing four different couple of accelerometers: two couples among x-axis (positions 1-6 and 7-10) and other 2 couples among y-axis (positions 1-6 and 3-9). The In x-direction the phase velocity tends to the value of 700 m/s. This result shows a good match

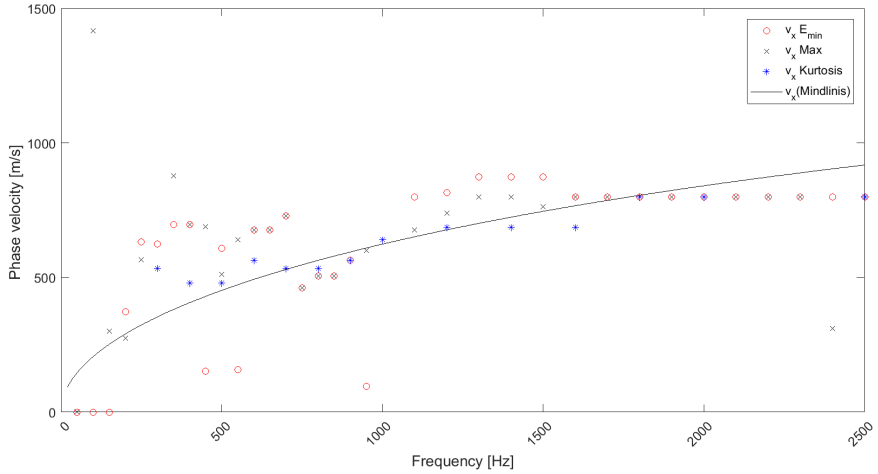

Figure 4.7: Comparison between Minimum Energy, Maximum and Kurtosis Methods - Dispersion curve on x-axis

with the theoretical Mindlin's dispersion. Rather than the other two aforementioned method, the Kurtosis criteria shows a good result for frequencies lower than 500 Hz. The statistic deviation of the values is small and matches quite well with the theoretical phase velocity course. Even analyzing the y-axis, the result match well with the theoretical dispersion curve.

ToF algorithms observations

A Limit of the Tof algorithms is related to the determination of the onset signal due to the high number of reflections coming from the edges of the CLT panel. As the reflections increase, the onset signals is harder to detect. Comparing the three methods discussed above, the Kurtosis shows a better description of phase velocity and returns more homogeneous value. Looking in Fig. 4.7 where phase velocity results are compared in the x-axis, it can be seen how maximum and energy minimum methods show more fluctuating results rather than kurtosis methods, which shows more homogeneous values. Therefore the analysis of the phase velocity using more methods is useful for the correct recognition of the dispersion curve. Once the dispersion curve is known, wavenumbers can be derived. The analysis of the wavenumbers gives credit to the result of the radiation efficiency found with the DCM and CSTB methods. Fig. 5.1 shows that the coincidence frequency (found at the crossing between acoustic wavenumber and structural wavenumber) has two values around the frequency of 300-500 Hz, that has a match with the higher value of radiated sound power. The presence of two coincidence frequencies

is due to the orthotropic characteristics of the CLT, but while the numerical estimation gives defined frequency, the experimental result are not as much clear.

4.5 Phase shift method

The measurement setup mounted for the implementation of the Phase shift method is the one shown in Fig. A.4. The spacing between the receivers is important for the resolution of the method: the shorter the spacing of the accelerometers, the higher the definition. This method allows to determine the dispersion curve and to identify frequency modes. The phase shift method is generally applied in the seismic frequency range where modes are better visualized rather than finite plates, where a lot of reflections occur.

The image scattering is due to the reflection from the edges of the CLT plate. Firstly two image dispersion were found: one in the x-axis and the other in the y-axis in the first panel, that can be seen in Fig. 5.2. Image dispersion in the two axis differ due to the orthotropic behavior of the CLT plate. In this case it can be seen that the influence of reflections is more relevant in the y-axis. This is due to several facts: first, that the slab is made of four panels, y being the shorter dimension of each of those; second, within each lamella, the and to the fact that there is a space exiting between two adjoining lamellas, where reflections happens. Thinking on how a CLT panel is made, a great number of reflections will be expected. Thus Fig. 5.2 (b) rightly appears to have more reflections than 5.2 (a). An observation should be made: the phase shift allows us to understand when reflections occur, therefore is possible to better understand the fluctuation of dispersion curves evaluated with the ToF methods. Picking the maximum value from the Fig. 5.2 the dispersion curve can be constructed and then it is possible to evaluate the structural wave number.

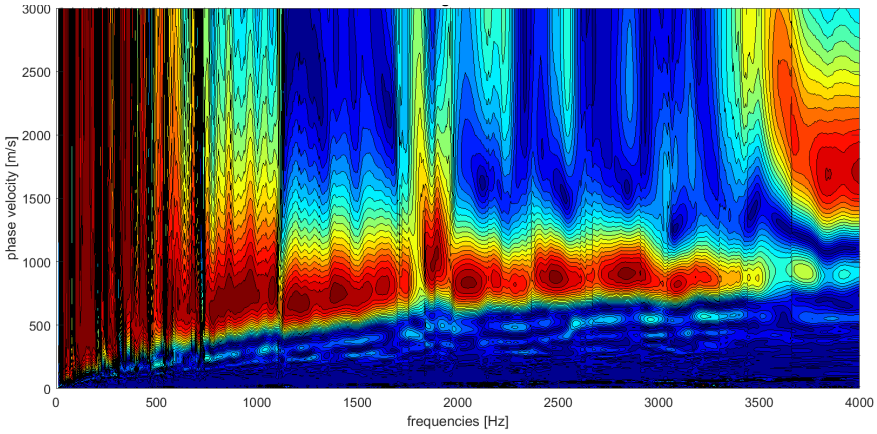

(a) Image dispersion of x-axis

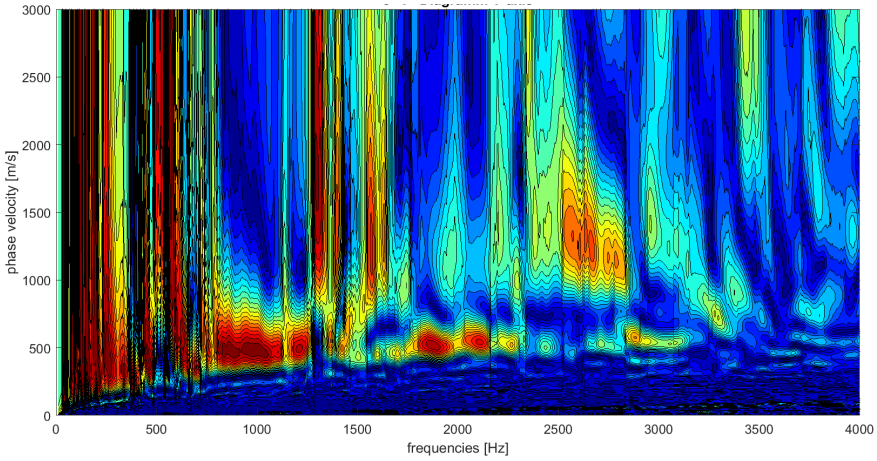

(b) Image dispersion of y-axis - panel 1

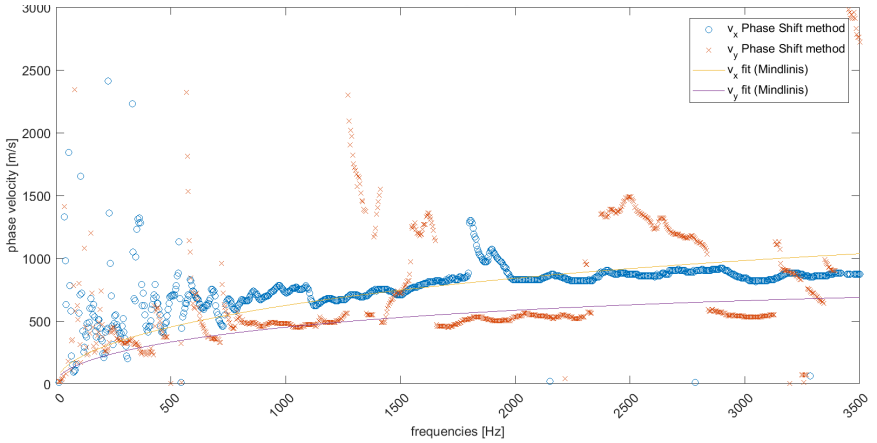

(c) Dispersion curves

Figure 4.8: Phase shift method

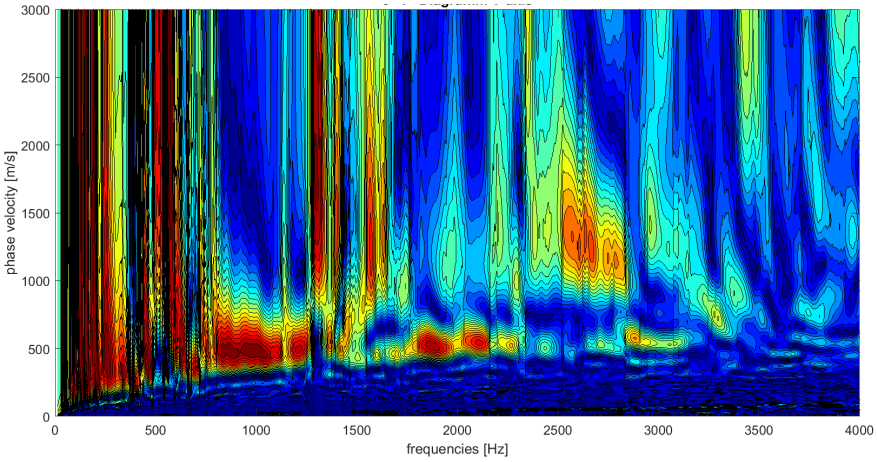

(a) Dispersion Image on y-axis - panel 1

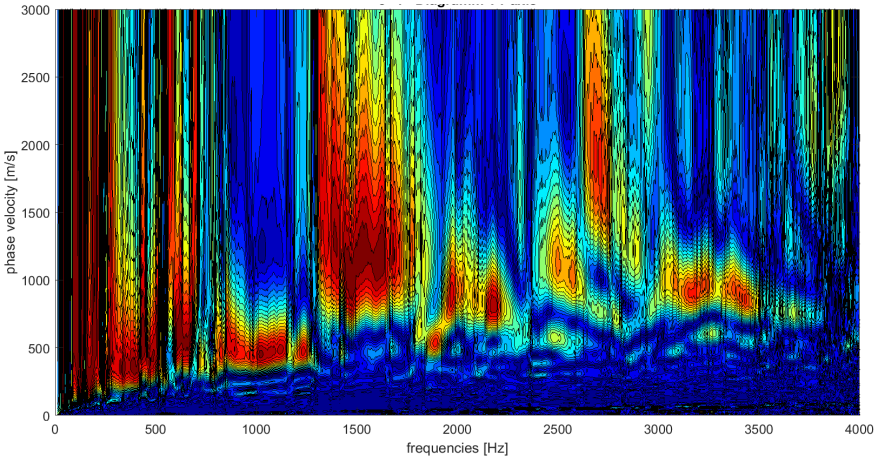

(b) Dispersion Image on y-axis - panel 2

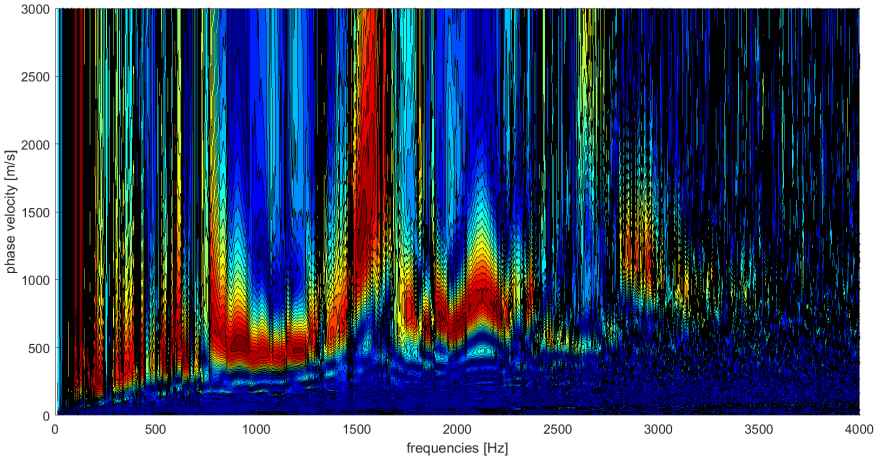

(c) Dispersion Image on y-axis - panel 3

Figure 4.9: Phase shift method

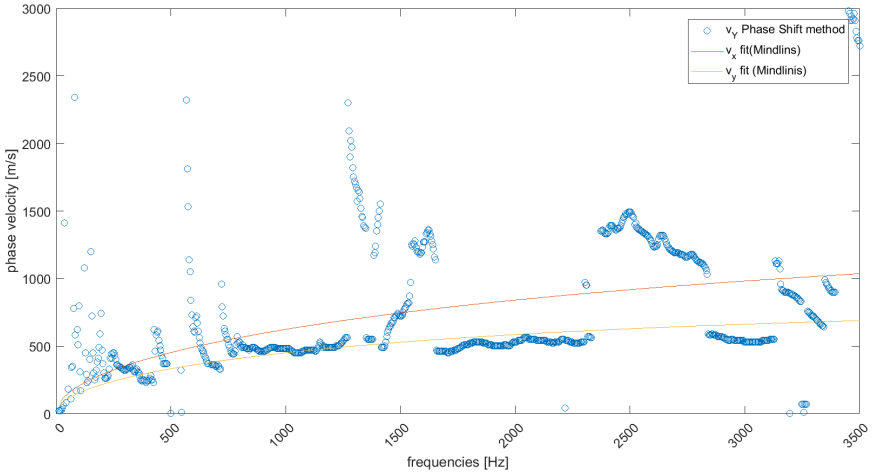

(a) Dispersion Curve on y-axis - panel 1

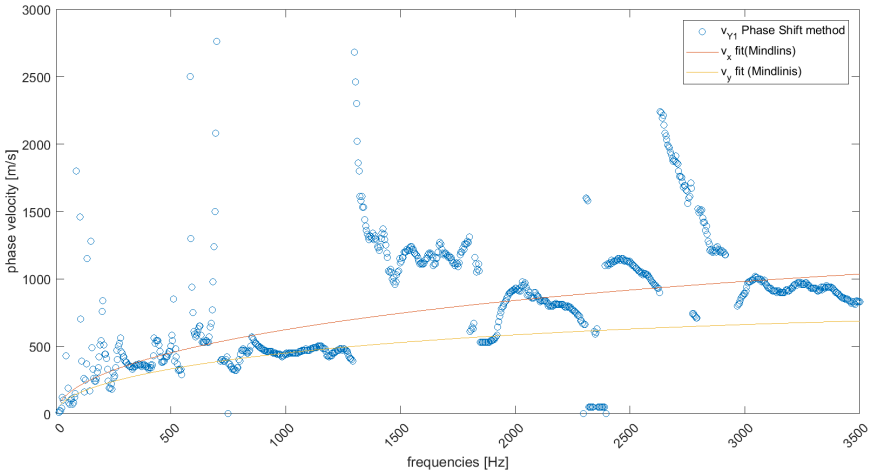

(b) Dispersion Curve on y-axis - panel 2

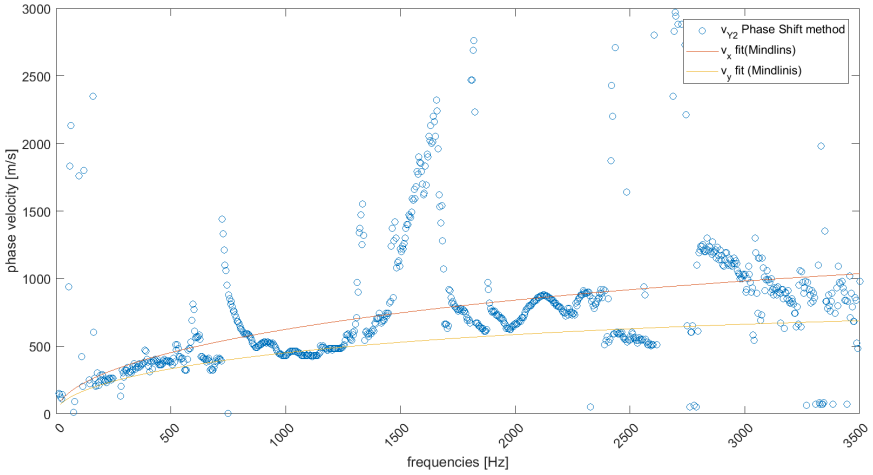

(c) Dispersion Curve on y-axis - panel 3

Figure 4.10: Phase shift method

Chapter 5

Discussion of the results

5.1 Phase velocity observations

The phase shift methods presents a better visualisation of the image dispersion; some comments and observations can be drawn from the Fig 5.2. First of all, the reflections can be easily seen, resulting in the non-defined shape of the image. This explains why the ToF algorithms do not always work properly: as the number of reflection increases, the error on evaluating onset signal occurs. Secondly, it can be seen that among the different energetic content of the signal, the most powerful in the low frequency range is associated with the fundamental mode and all the other energetic part can be associated to higher modes. Modal behaviour can be seen by plotting the amplitude spectra of the signals recorded with the grid of 150 receivers. Fig. 5.3(a) shows the motion of the plate when excited by the shaker at the frequency of 40 Hz: analyzing the picture it can be understood that at that frequency the plate reaches the first mode. Looking at the zoomed dispersion image in the x-axis, Fig. 5.2(c), it can be noted that at that frequency a maximum is found. Thus as a first approximation we can relate the maximum value of the dispersion curve, found with phase shift method, with a vibration mode. Analyzing the frequency in the image dispersion where maxima occurs, from 0 to 440 Hz (coincidence frequency), it can be found that the peaks correspond to a kind of vibration modes, even if is not so detailed. Modes of vibration from 40 Hz to 448 Hz can be seen in Fig.5.3,5.4,5.5. Should be noted that, taking 40 Hz as an example, phase velocity reaches a maximum for all the phase velocities investigates: this can be explained knowing how the phase shift method works. In fact, summing up the amplitude values of more shifted wavelength among a slope, many phase velocities will reach a maximum, because signals matrix will always have one element that has

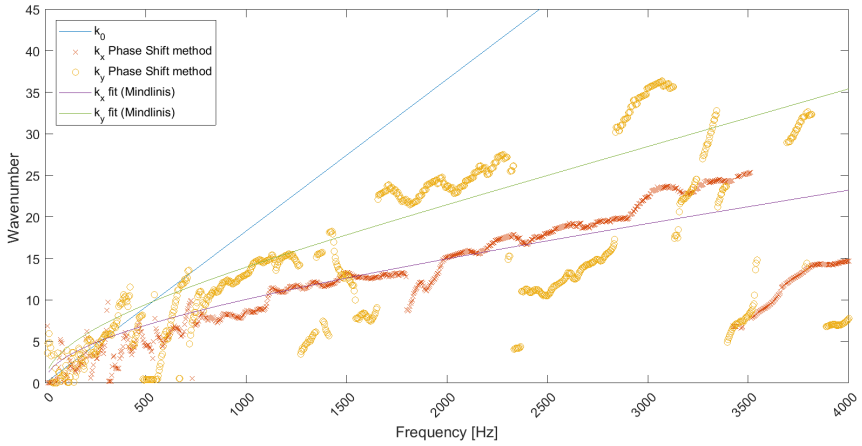

Figure 5.1: Wavenumber - Phase Shift Method

great value.This phenomena occur in fact for low frequencies.
Comparing the result of phase shifts among the x- and y-axis, respectively Fig.5.2 a and b, it can be noticed that more reflections appears in the y-axis. This can be explained due to the composition of CLT panel: on the x-axis the accelerometers are all on the same lamella, while on y-axis the accelerometers are placed in different adjacent lamellas. Thus the direct path in y-axis could not travel among the same upper lamella, therefore this helps to create reflections and worst image dispersion. This can help to explain the fluctuating values in y-axis where phase velocity appears to rapidly change in a small frequency range: for example at 1500 Hz. Analyzing the dispersion curve in the y-axis in the three panels it can be seen how reflections influence the dispersion image. In this case the reflections appears due the join existing between the panels constituent the plate. Fig. 4.10 shows greater scattering of the results as the distance from the source to the receiver increases: Fig 4.10 (c) gives no identifiable trend above 2500 Hz. Results shown in Fig. 4.10 (a) have a more homogeneous trend and values closer to the theoretical ones compared to the results found in panel 2, shown in Fig. 4.10 (b), even if some time fluctuating results occur.

5.2 Wavenumber observations

In the previous section the signal was analyzed in order to evaluate the phase velocity so that wavenumber could be estimated. The analysis of the wavenumbers allows us to better understand the sound property of the CLT plate. Due to its orthotropic behavior, we aspect to visualize two coincidence

frequencies. Knowing the dispersion curves, the structural wavenumber can be obtained from Eq. (2.23) and also acoustic wavenumber can be found by substituting $c_0 = 343.8$[1] into phase velocity variable. Therefore, the coincidence frequency can be visualized as the interaction of the acoustic wavenumber curve with the measured one. Using the dispersion curve found with the phase shift method, wavenumbers can be seen in Fig. 5.1. The coincidence frequencies occur around 300 Hz and 500 Hz. On the y-axis it can be seen that the wavenumber does not follow the theoretical curve as well as in the x-axis because the reflections provide a bad resolution even for the wavenumber calculation. Moreover as the frequency increase, the match is poorer. Looking at the Fig. 5.8, it can be better understood how reflections influence the result. From panel one to panel three the values shows a decreasing definition; as we can see in Fig. 5.8 (c), above 2500Hz we are not able to define a trend. This can be due to the reflections from the edges of the panel, as already said, and even to the internal loss damping that can shift the phases of the signals. To better analyze the behavior of the element, the imaginary part of the signal should taken into account. Other results are shown in Fig. 5.6 obtained with the ToF algorithms for the x axis and in 5.7 for the y axis. The results obtained with all the methods discussed in chapter 3 show a good agreement with the theoretical dispersion curve evaluated with Eq.(2.44), even if some results are not correct in the whole frequency range analyzed.

[1]In fluids there is no dispersion of phase velocity thus the velocity assume just one value for all the frequencies

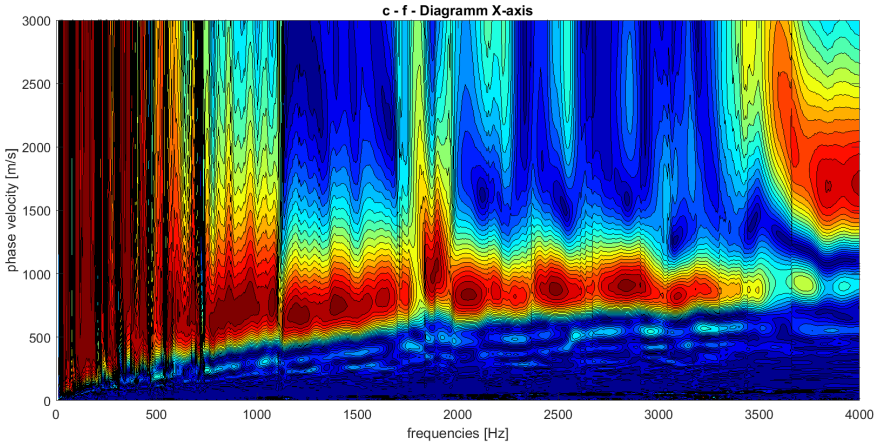

(a) Image dispersion of x-axis

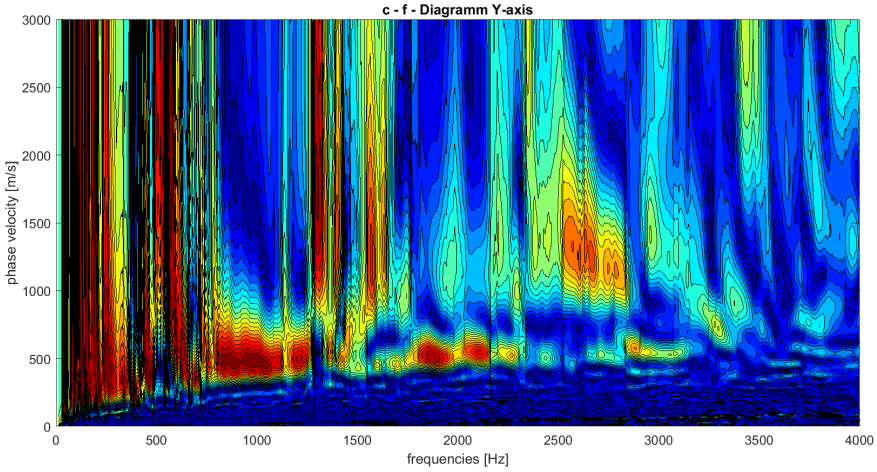

(b) Image dispersion of y-axis - panel 1

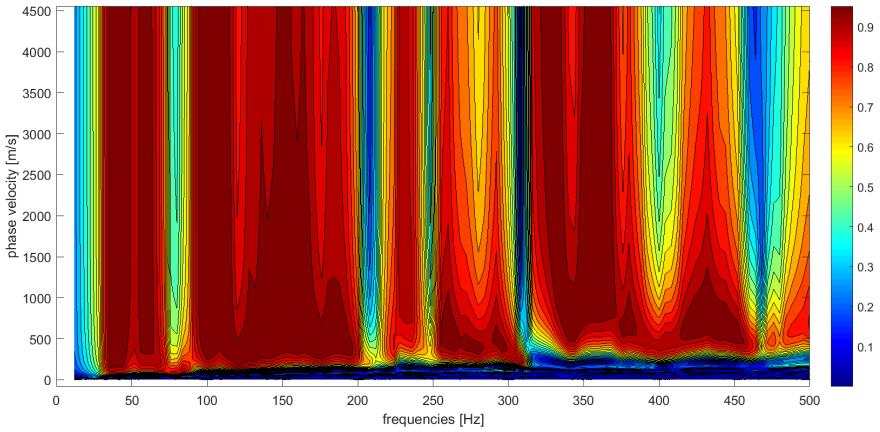

(c) Zoomed image dispersion of x-axis

Figure 5.2: Phase shift method

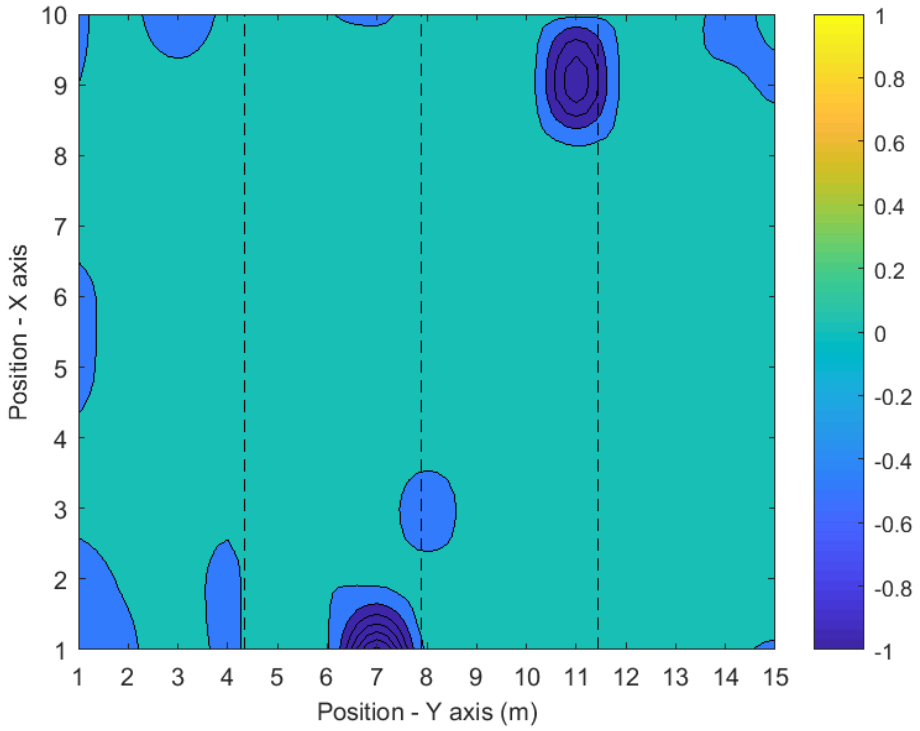

(a) Vibration velocity at 40 Hz

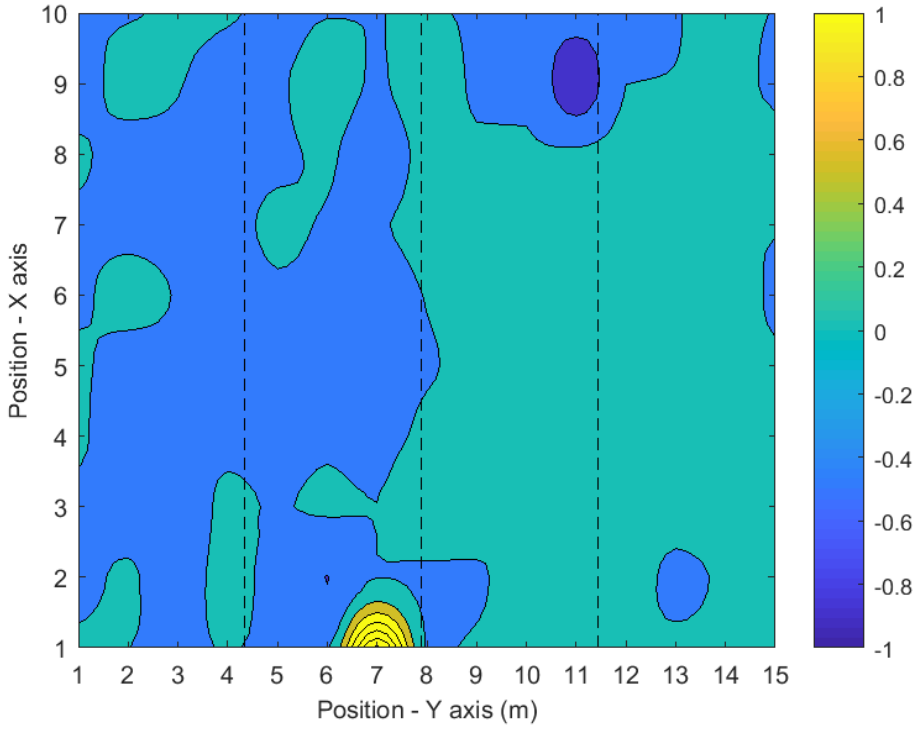

(b) Vibration velocity 60 Hz

Figure 5.3: Plate vibration distribution

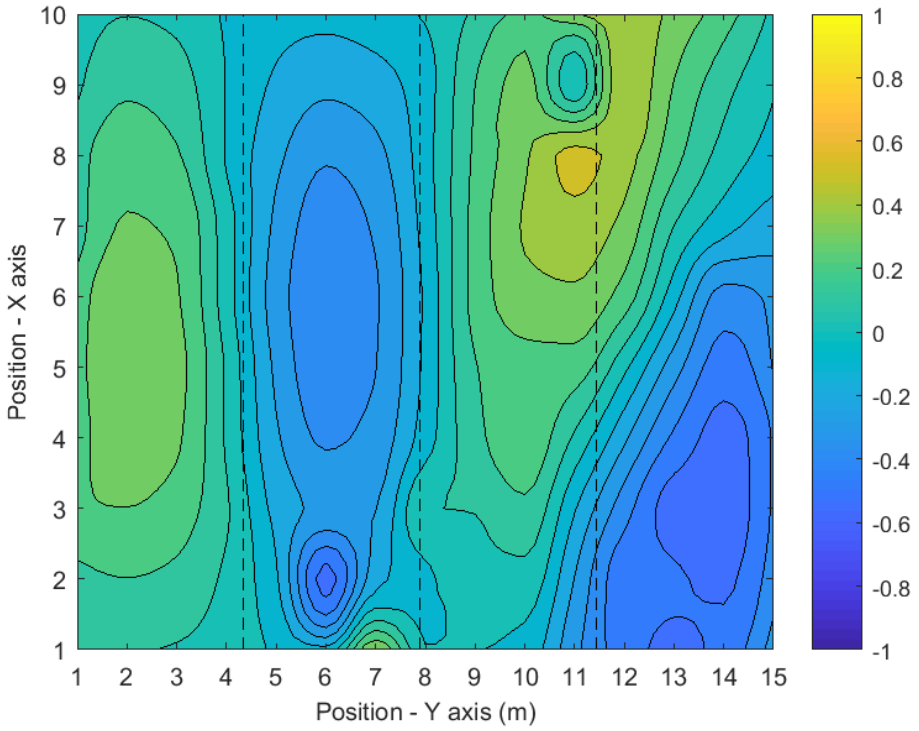

(a) Vibration velocity at 100 Hz

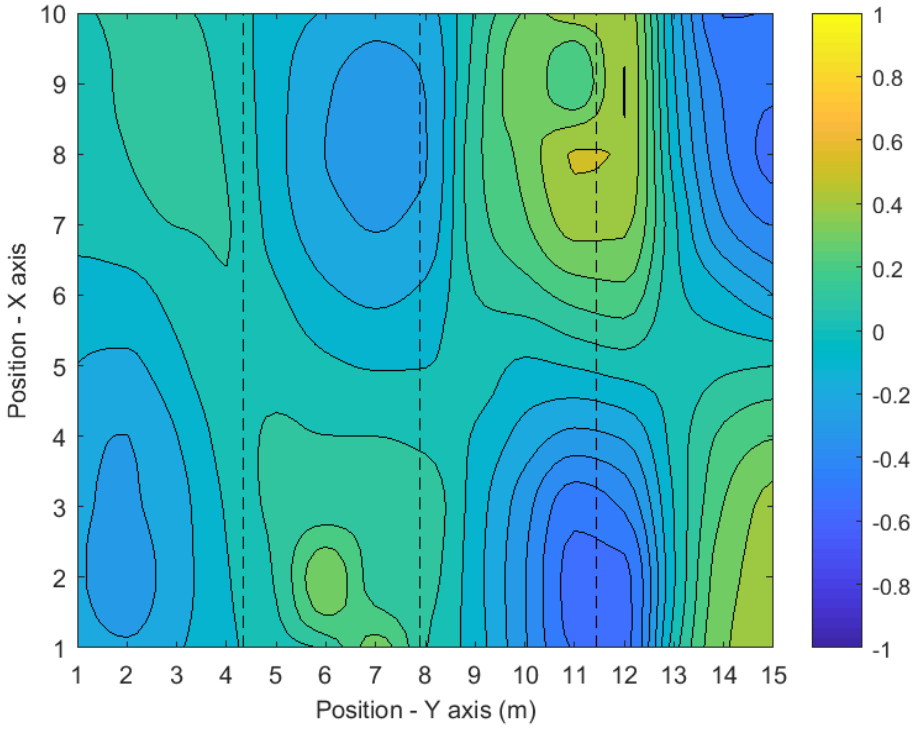

(b) Vibration velocity at 140 Hz

Figure 5.4: Plate vibration distribution

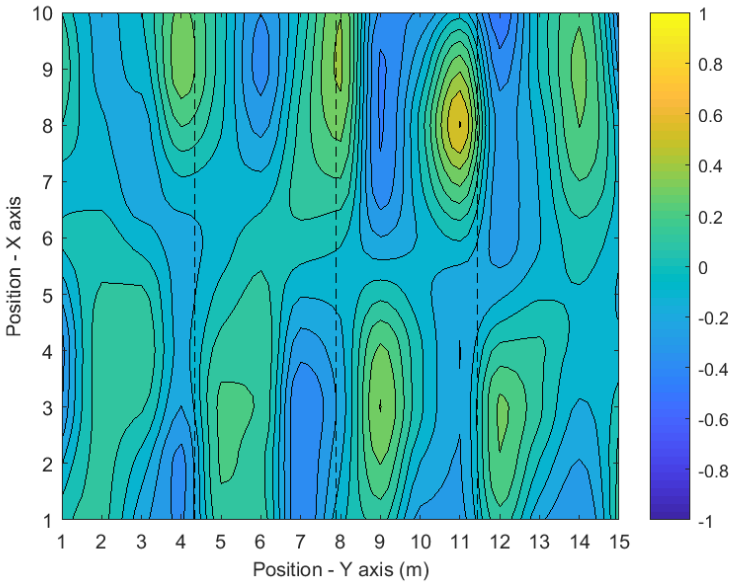

(a) Vibration velocity at 348 Hz

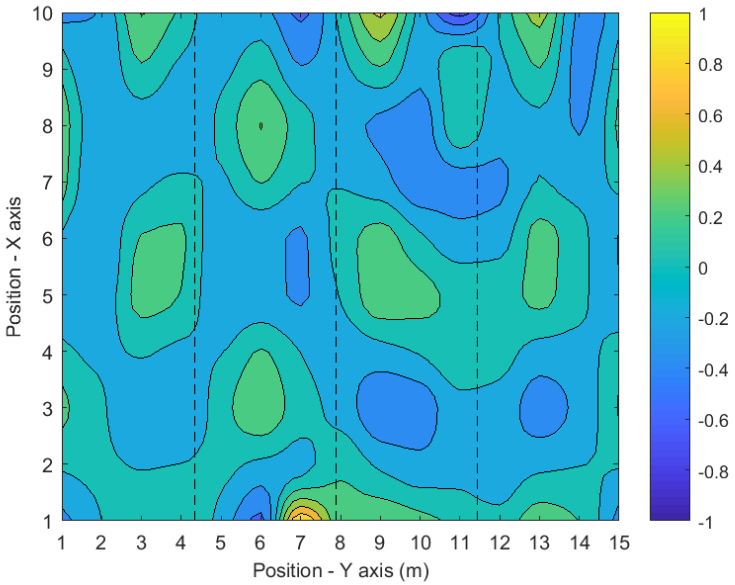

(b) Vibration velocity at 448 Hz

Figure 5.5: Plate vibration distribution

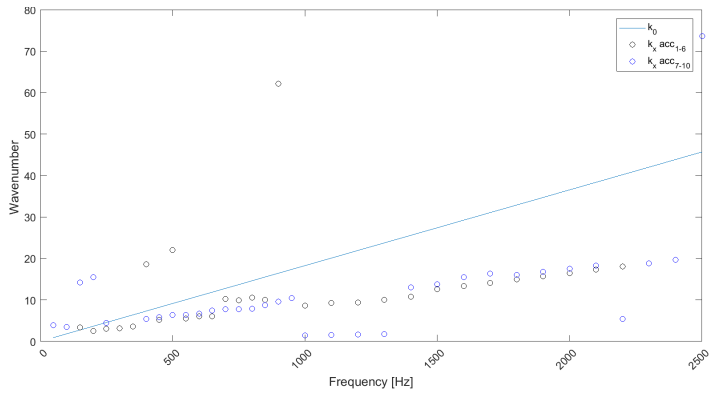

(a) Wavenumber on x-axis - Minimum Energy

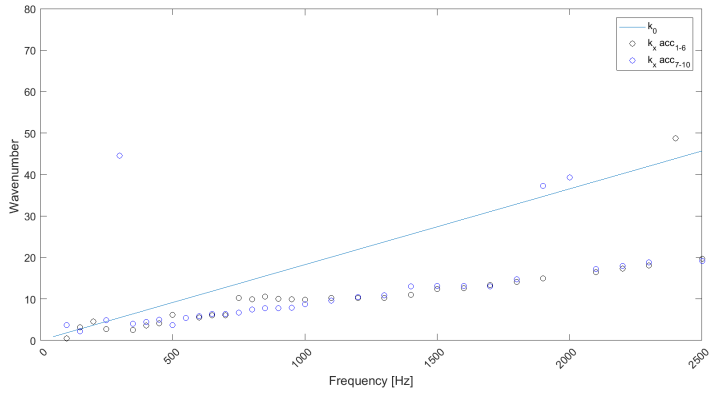

(b) Wavenumber on x-axis- Maximum peak

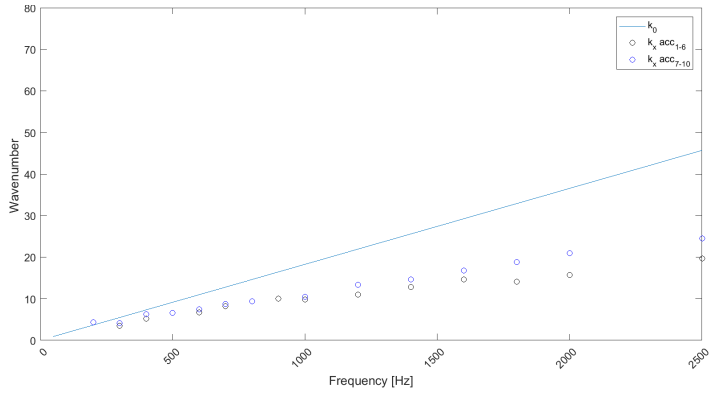

(c) Wavenumber on x-axis - Kurtosis

Figure 5.6: Wavenumber on x-axis - ToF algorithms

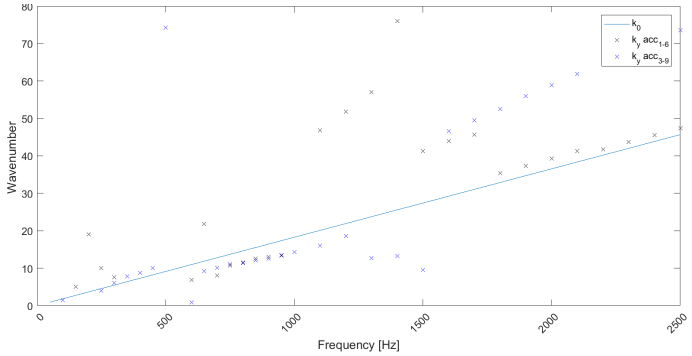

(a) Wavenumber on y-axis panel 1 - Minimum Energy

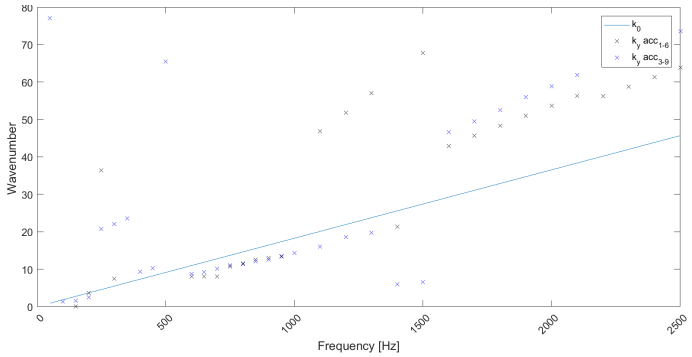

(b) Wavenumber on y-axis panel 1 - Maximum peak

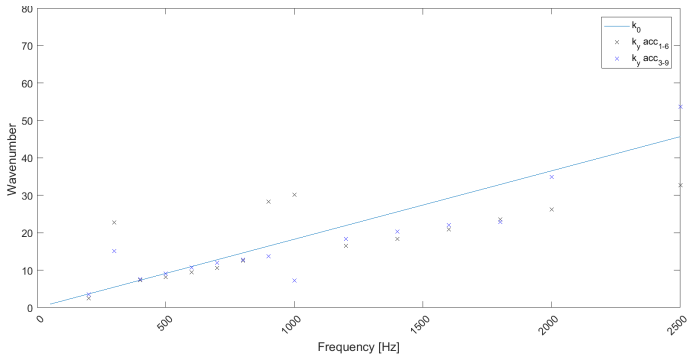

(c) Wavenumber on y-axis panel 1 - Kurtosis

Figure 5.7: Wavenumber on y-axis panel 1 - ToF algorithms

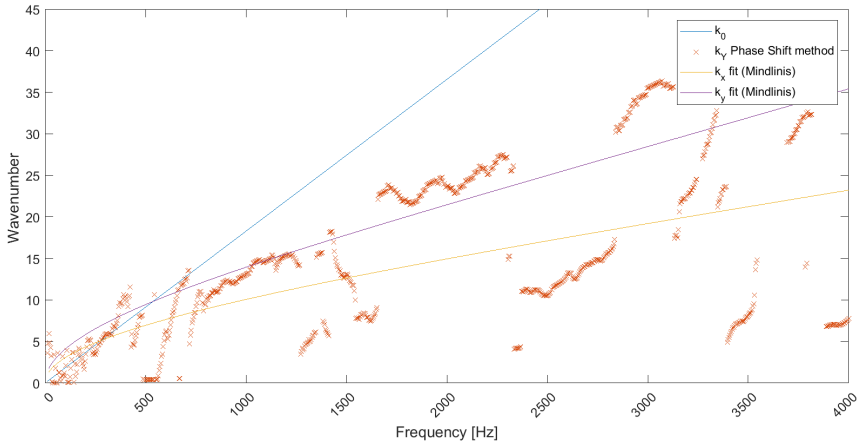

(a) Wavenumber on y-axis - panel 1

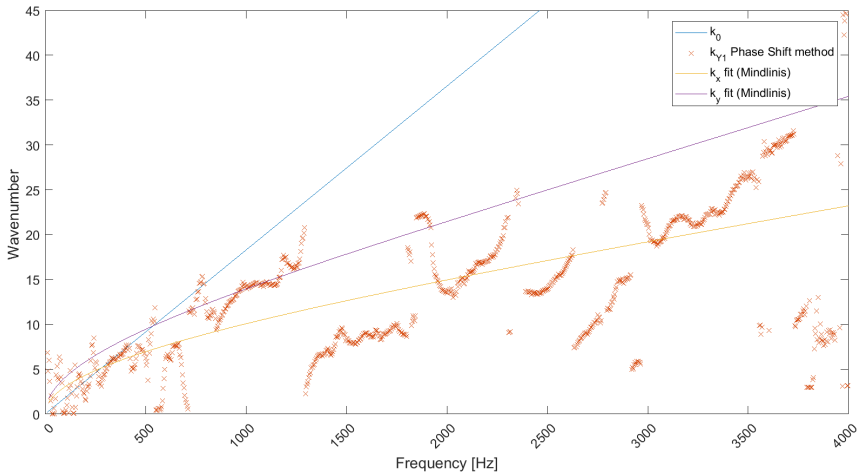

(b) Wavenumber on y-axis - panel 2

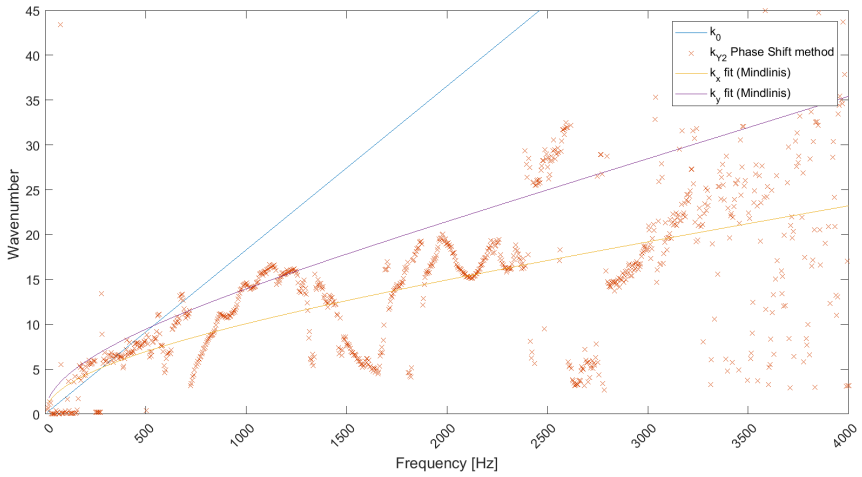

(c) Wavenumber on y-axis - panel 3

Figure 5.8: Phase shift method

Chapter 6

Conclusions and future work

CLT structures are gaining success due to their extraordinary performance in terms of seismic behaviour, thermal efficiency, velocity of installation and fire resistance. As it concerns the acoustic behaviour, the high stiffness of the CLT elements together with the low thickness, and therefore low mass, do not provide the best conditions to guarantee a good sound insulation, and this problem is often a complain among people that live in sulti-storey CLT buildings. Therefore it is extremely important to know the vibro-acoustic behaviour in order to implement the most effective mitigation strategy and find the construction solutions optimized for CLT also from the acoustic side.

The main goal of this thesis is to understand how CLT panels radiates sound power and to identify the critical frequencies of the panel. Two main parameters have been investigated through experimental measurements and theoretical models: the coincidence frequency and the radiation efficiency.

At the coincidence frequency, each element suffer from a sharp diminishment of sound insulation, sharply diminished. While for standard construction materials the critical frequency occurs in either very high (gypsum board) or very low (masonry, concrete) frequency ranges, the critical frequency in CLT falls into a frequency range which is easily excited from environmental source and to which the ear is particularly sensitive, therefore much effort should be done to identify correctly that frequency. In this work, the coincidence frequency was analyzed through the determination of the dispersion curves in the two principal directions and finding the crossing point between the structural wave number and the wavenumber in air. The dispersion curves have been obtained experimentally through methods that evaluate the time of flight (Maximum peak, Minimum energy, Kurtosis) and the Phase Shift method. Dispersion curves shows that the CLT panel is working as an orthotropic plate, as expected. Analyzing the image dispersion found with the phase shift method is possible to relate the modal vibration of

the plate to the maximum peaks found in the image. Since the results of the phase shift method have been calculated in one direction, the modal behavior of the plate and the dispersion image are not fully matching. Comparing the results of ToF algorithms can be found that the three methods gives a good compatibly with phase shift method result. Anyhow could be observed that Tof results slightly differ between each other. Maximum peak and Minimum Energy methods present more fluctuating results than Kurtosis, thus its appears to better recognized the onset signals than the others.

Radiation efficiency is the parameter taken into account to relate the vibration motion to the radiated sound power: at the coincidence frequency, the radiation efficiency reaches the unit. At present no standard procedures are defined to evaluate these parameters, thus in this thesis we referred to different procedures taken from the literature, in order to compare the results. DCM and CSTB method were taken into account. Radiation efficiency is related to vibro-acoustical behavior of the plate, which is linked to the properties of the panel. DCM and CSTB methods shows a good agreement in evaluating the radiation efficiency: moreover the analysis conducted on the dispersion curves has proven that the results of the DCM and CSTB methods are correct. Slightly different modal behavior is noted when two different kind of input signal are fed to the shaker for the DCM method; anyhow the overall behavior is the same. The DCM method provides the advantage that the measurements are not influenced by the acoustic characteristics of the environment where measurement were carried out: the results are calculated from the vibration velocity of the plate which are not influenced by the acoustic response of the room. On the other side, the CSTB method requires a good diffuse field into receiving and exciting rooms: the method take into account the pressure level which is recorded by sounds meter level, so acoustic response of the rooms influence the result. If on the one side the DCM provides results which are independent from the from acoustical response of the environment, the measurements that need to be done are extremely time-consuming, while the CSTB method gives good results with simple measurements and less computational effort.

The future work could regard the integration of the results taken from the two principal direction of orthotropy and evaluate the modal vibration of the plate; once the modal vibration velocity is known, the radiated sound power can be estimated by using the analytical expressions. Working on this way, radiation efficiency can be found using two string of accelerometers rather than 150 point grid or the equipment needed for the CSTB method, that means faster, cheapest and more robust measurements. Another future work could be to gain better understanding the details of the dispersion image in order to evaluate the properties of the structures. High frequency

could be used to analyzed the changing in impedance due to the boundaries of the lamellas and the presence of inhomogeneities. One of the features that deserve a deeper insight is finally the fluctuation of the wavenumber, especially on the y-axis; this could be due to the presence of a low frequency lamb wave which is traveling among the upper layer of the CLT lamellas or could be just a numerical artefact. This interaction can be also approached through the analysis of the phase shift image, where maximum peak are slightly shifted in frequency considering the three panel on the y-axes. This work has provided a starting point on the analysis of the acoustical properties of CLT plates with encouraging results that could be developed in many ways in order to gain a deeper knowledge of how waves propagate in the CLT elements and are radiated in the surrounding environment.

Appendix A

Figure Captions

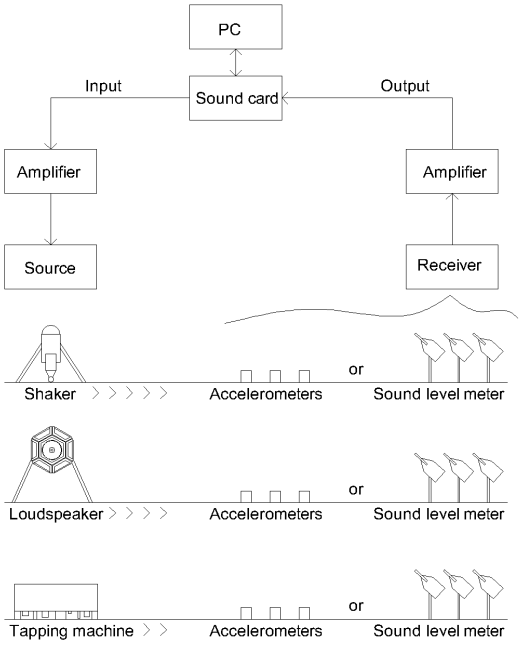

(a) Measurement chain

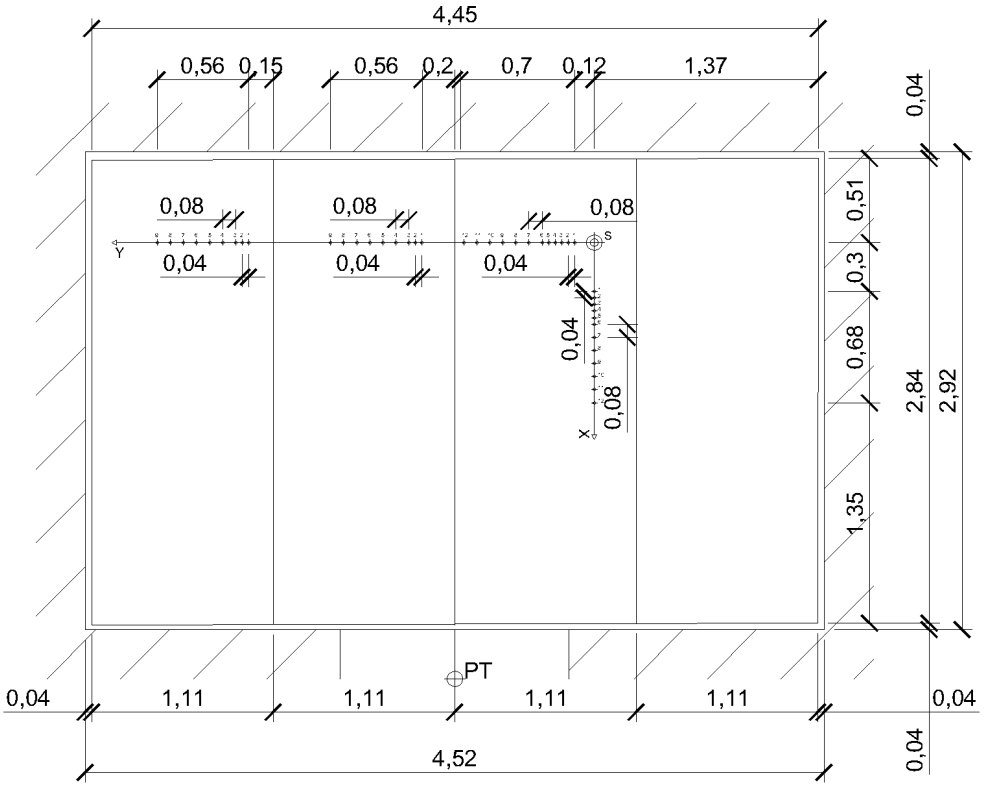

(b) ToF measurement set up

Figure A.1: Measurement

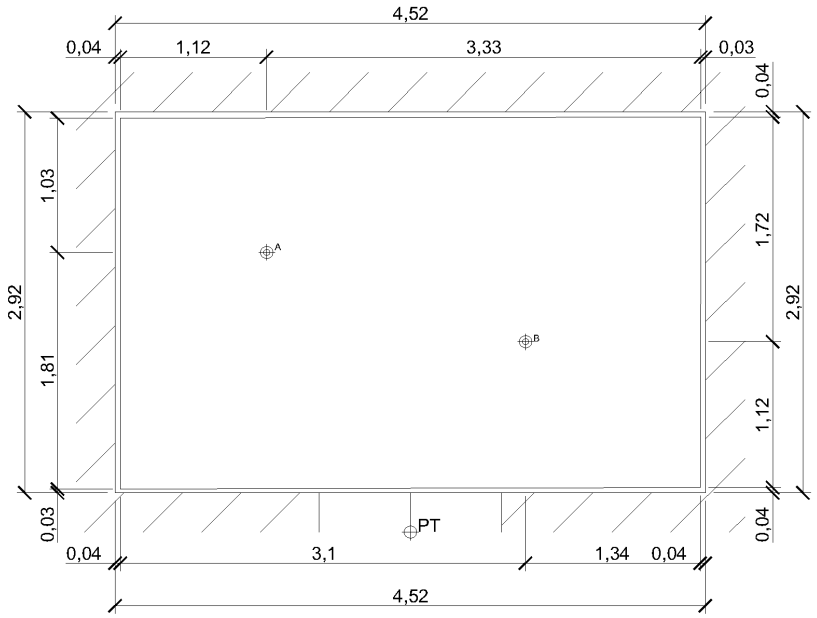

(a) Accelerometers positions

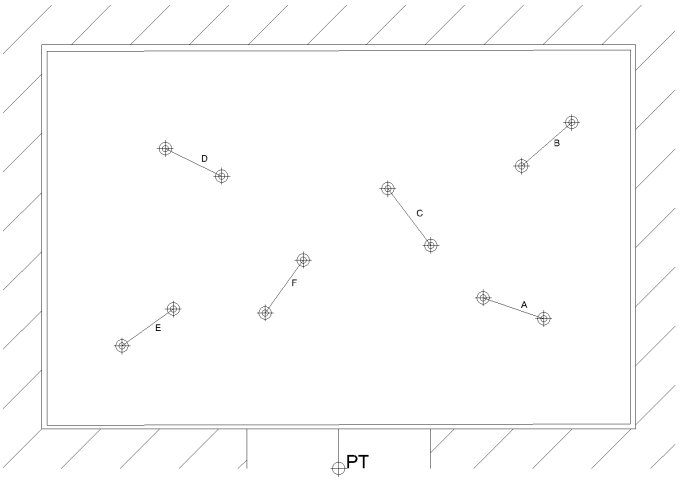

(b) Tapping machine positions

Figure A.2: Receiving position for CSTB method

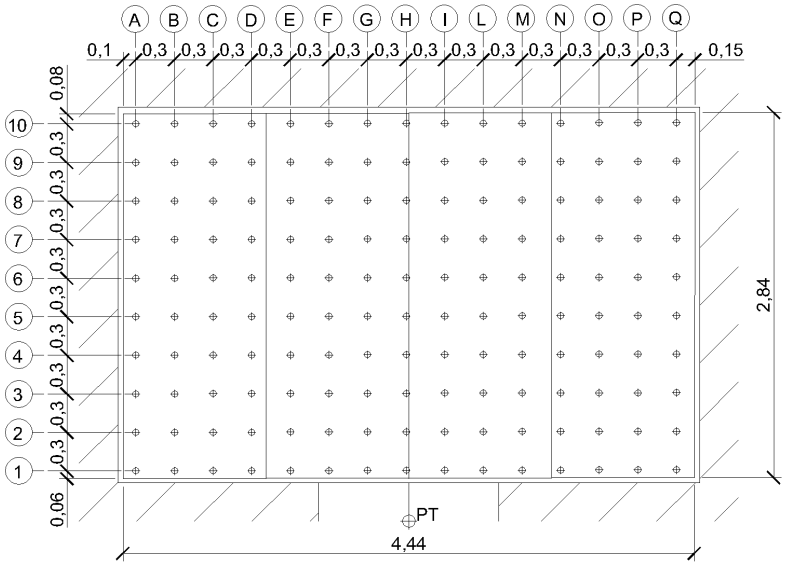

Figure A.3: DCM method: accelerometers position

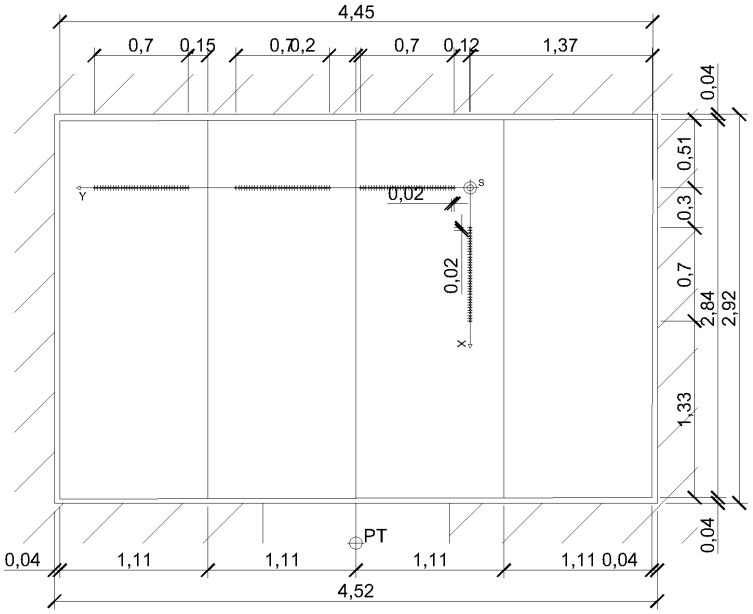

Figure A.4: Phase shift method: accelerometers position

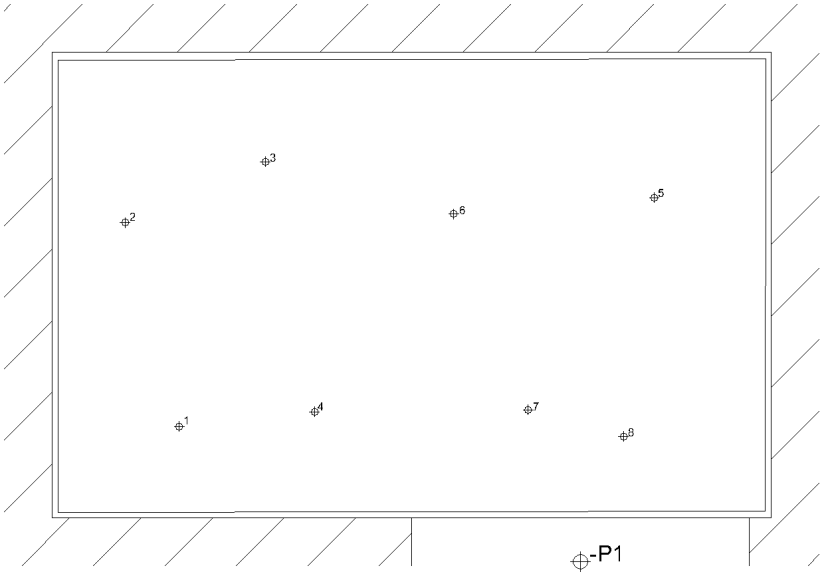

(a) Accelerometers positions

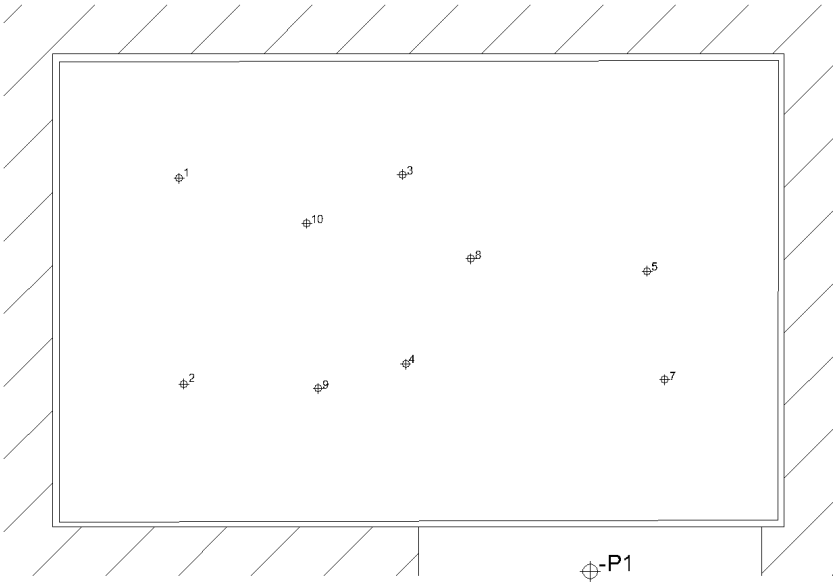

(b) Sound-meter level positions

Figure A.5: Receiving position for CSTB method

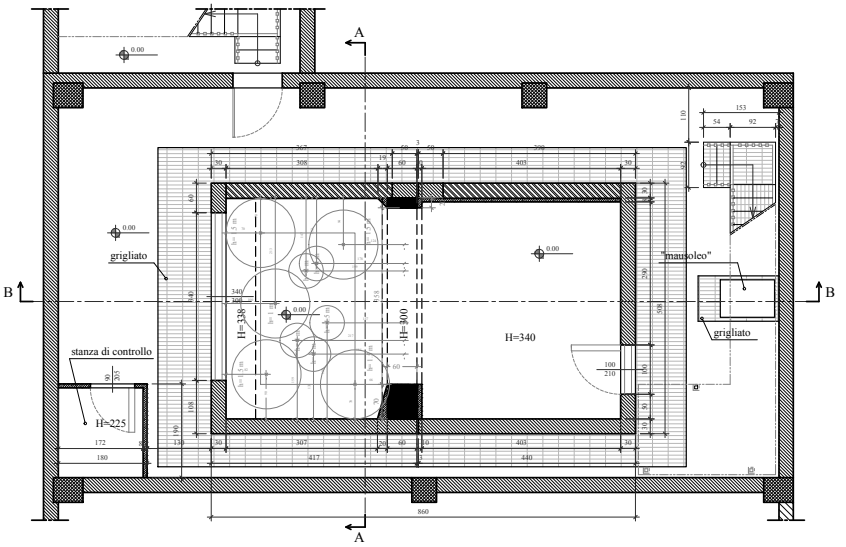

PIANTA LIVELLO -1

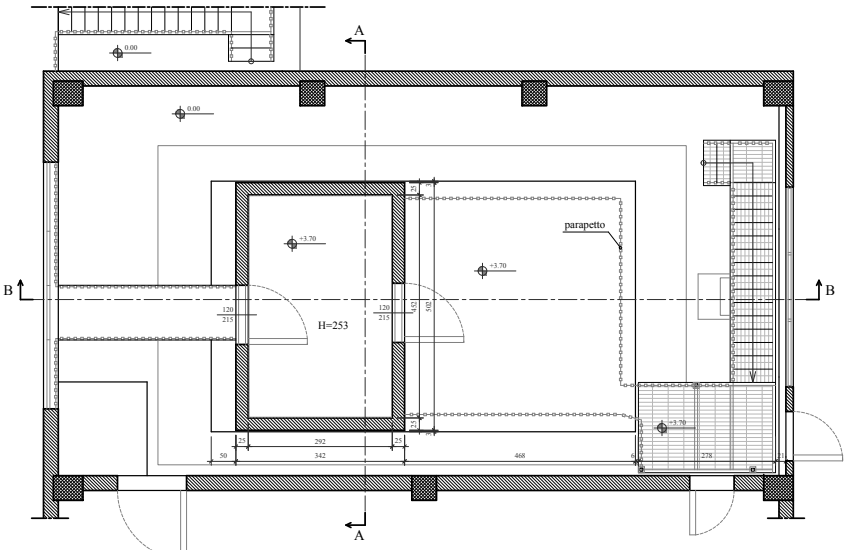

PIANTA LIVELLO 0

Figure A.6: Acoustic transmission chambers

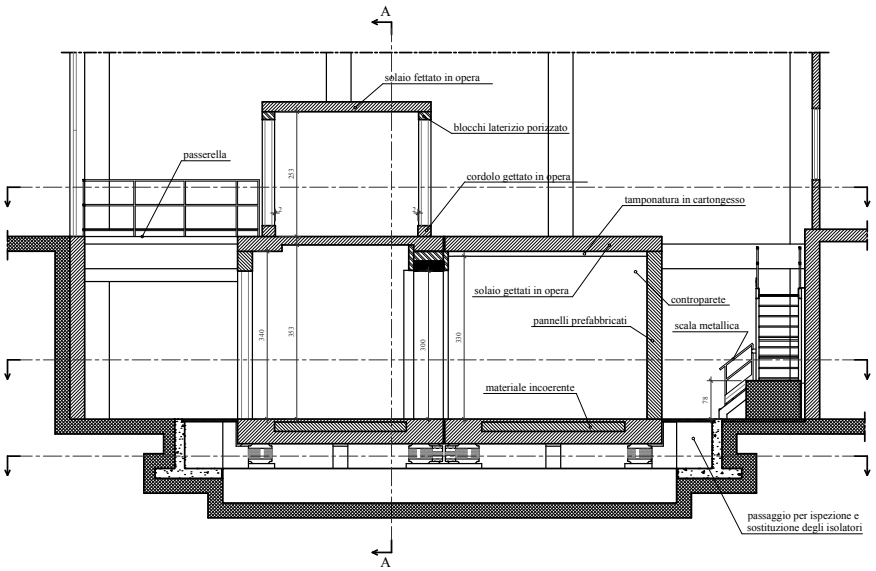

SEZIONE LONGITUDINALE B-B

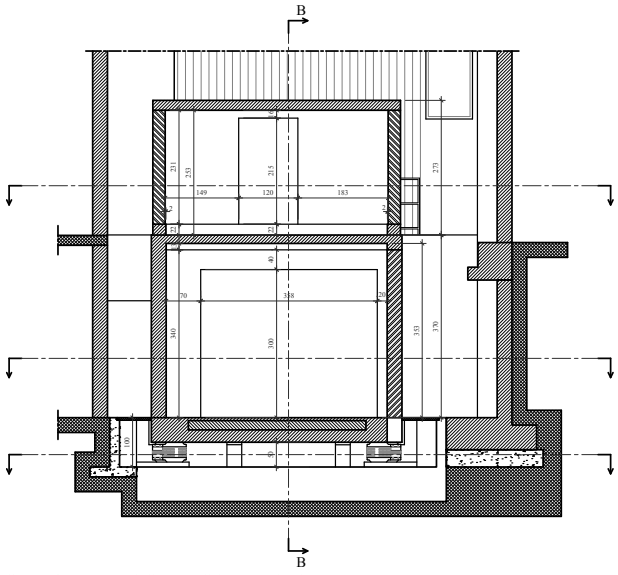

SEZIONE TRASVERSALE A-A

Figure A.7: Acoustic transmission chambers

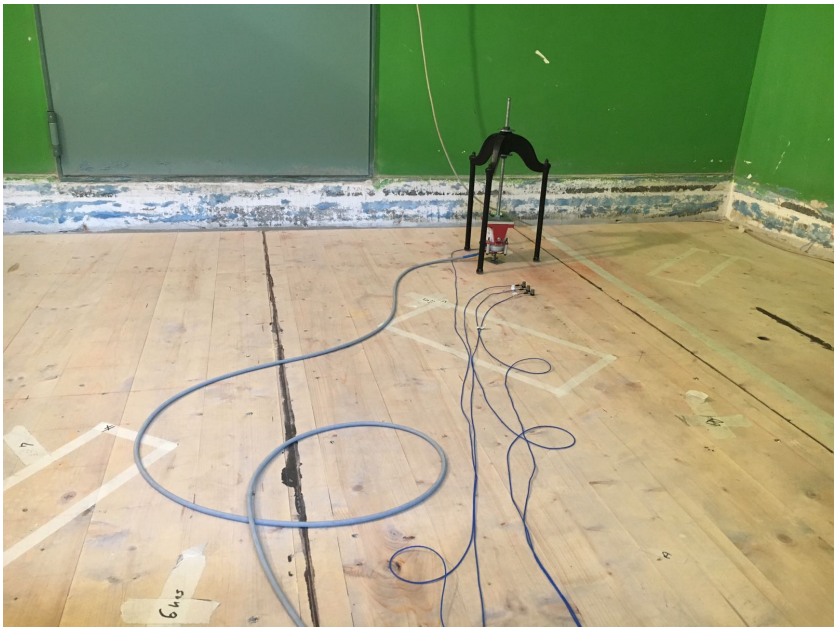

(a) Shaker and accelerometers in the source room

(b) Sound meter level in the receiving room

Figure A.8: Receiving position for CSTB method

Appendix B

Comparing Radon and phase shift transform

B.1 Example using synthetic data

In order to compare the two methods a mathematical model of two layered media will be developed; it will allow to calculate the reflection from the bottom of the layers and the direct path, for a given thickness of the layer (z_1, z_2) and propagation velocities (v_1, v_2).

Outline of the procedure. For comparing the two methods a step by step process will be used, in order to be sure about the results at each step.
Step one: consider just a semi-half space as model, in which the properties are homogeneus and the reflection from the bottom doesn't exist.
Step two: consider a model with a direct path, first reflection and second reflection from he bottom of the first layer and the bottom of second layer respectively.
Step three: consider a model with a direct path, first reflection and second reflection respecting from the bottom of the first layer and the bottom of second layer, respectively, adding the damping factor of each layer.

Step one - $\tau - p$ Transform. The aim of this step is to generate a virtual recorded signal to which apply the transform, in order to better understand the result. The physical situation is outlined in Fig. B.1, where the thickness and the velocity of propagation are known; the assumed mathematical model is the well-known mass-spring-damping one.

B.1.1 Result and discussion

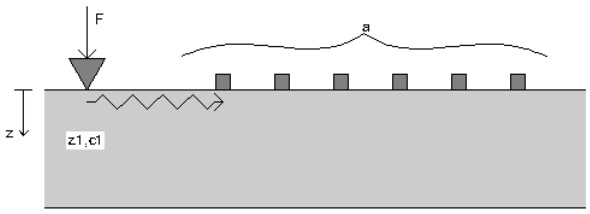

Figure B.1: Sketch of the physical situation assumed in step 1

in the case of $\omega_0 > \beta$ (hypothesis H.1), where ω_0 is the natural frequency, $\beta = \frac{c}{2m}$, c is the damping factor and m is the mass, the solution can be expressed as:

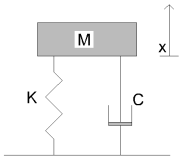

$$x(t) = u(t) = e^{i(\omega t - kx)} e^{-\beta t} \tag{B.1}$$

Therefore assuming:

- force frequency input $f = 100$ Hz,
- propagation velocity $v = 140$ m/s,
- skip distance between the geophones $dx = 0,2$ m,
- damping factor $\beta = 0$ (sinusoid),

the virtual signal can be calculated. Then, applying the '$\tau - p$ transform to the generated signal,the image result is shown in Fig. B.2. If we zoom in it, the result of Fig. B.2 can be seen, as expected. In fact, at the frequency of 100 Hz the maximum amplitude is at 140 m/s, as assumed before for the signal.

Step two - $\tau - p$ Transform. In this paragraph we consider the same model as before, but we add to the direct path the first reflection and second reflection, respectively from the bottom of the first layer and the bottom

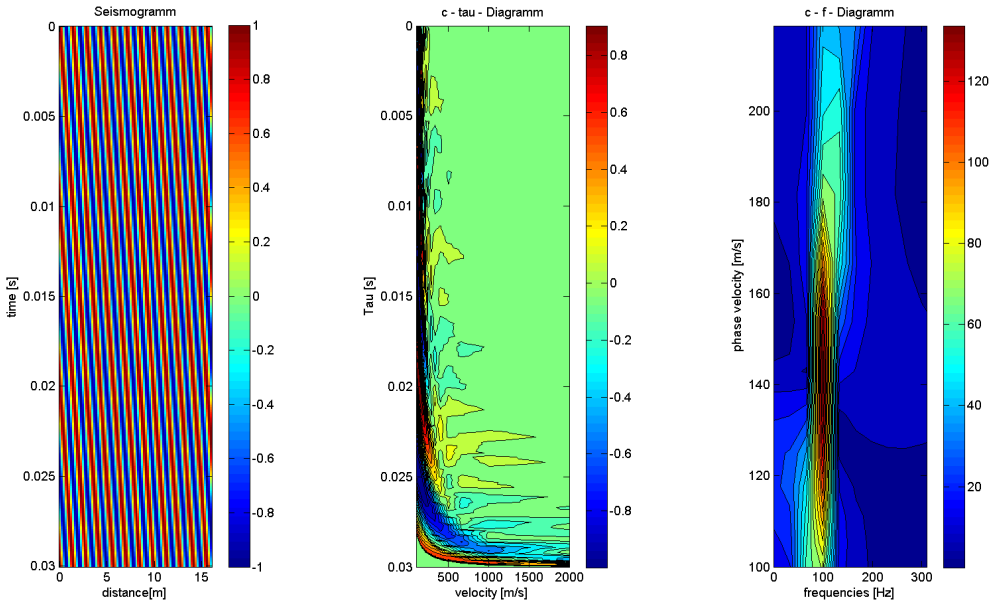

Figure B.2: Image dispersion zoom

of the second layer. For calculating the path time-delay an approximation should be done: the refraction angle between the two layered media is assumed to be zero, meaning that there is no bending for the ray-wave when it goes through the boundary between the two media. Considering this approximation the two time delays (first and second reflection) can be found out:

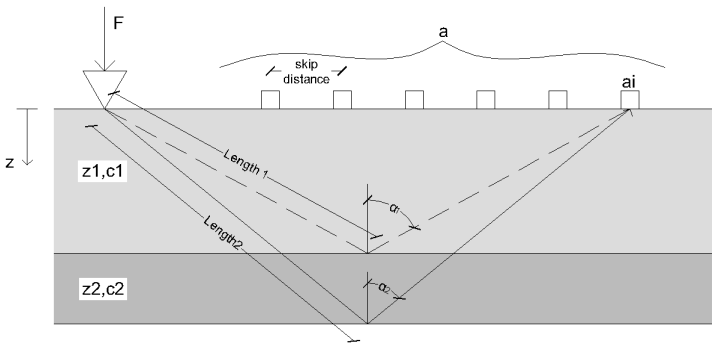

Figure B.3: Sketch of the physical situation assumed in step 2

$$t_{1,delay} = .\frac{2z_1}{cos\alpha_1}.\frac{1}{v_1} \tag{B.2}$$

$$t_{2,delay} = .\frac{2z_1}{cos\alpha_2}.\frac{1}{v_1} + .\frac{2z_2}{cos\alpha_2}.\frac{1}{v_2} \tag{B.3}$$

The first reflection can be calculated, using $t_{1,delay}$,as:

$$x(t)_{1,refl} = u(t) = e^{i(\omega((t-t_{1,delay})-kx)}e^{-\beta_1 t} \tag{B.4}$$

where β_1 is the coefficient of attenuation of the first medium. The second reflection can be calculated, using $t_{2,delay}$,as:

$$x(t)_{2,refl} = u(t) = e^{i(\omega((t-t_{2,delay})-kx)}e^{-\beta_2 t} \tag{B.5}$$

where β_2 is the coefficient of attenuation of the second medium.

$$u(t) = u(t)_{direct} + u(t)_{1,refl} + u(t)_{2,refl} \tag{B.6}$$

Setting the parameters:

- $z_1 = 0.1$ m, $z_2 = 0.15$ m,
- $v_1 = 140$ m/s, $v_2 = 230$ m/s,
- $\beta = 0, \beta_1 = 0, \beta_2 = 0$,

and applying the $\tau - p$ transform in this case it comes out the result in Fig. 2.2

It can be seen that in the image on the right, the Radon transform finds out two different velocities at the same frequency, as it should be, because the source input is the same and has a fixed frequency (100 Hz). Although two velocities are distinctly found, the value of the maximum amplitude doesn't correspond exactly to the velocity set in the input, but there is an error. This shows a limit of this transform that will be discussed below.
As the signal recorded by a geophone is discrete, it can be represented by a column vector with N values; the length of this vector corresponds to the recording time multiplied by the sampling frequency:

$$u_i = \begin{bmatrix} x_1 & x_2 & \cdots & x_N \end{bmatrix} \tag{B.7}$$

where $N = t_{totalrecorded} f_s$ and each row describes a transcript record of one geophone, so that for a M geophones:

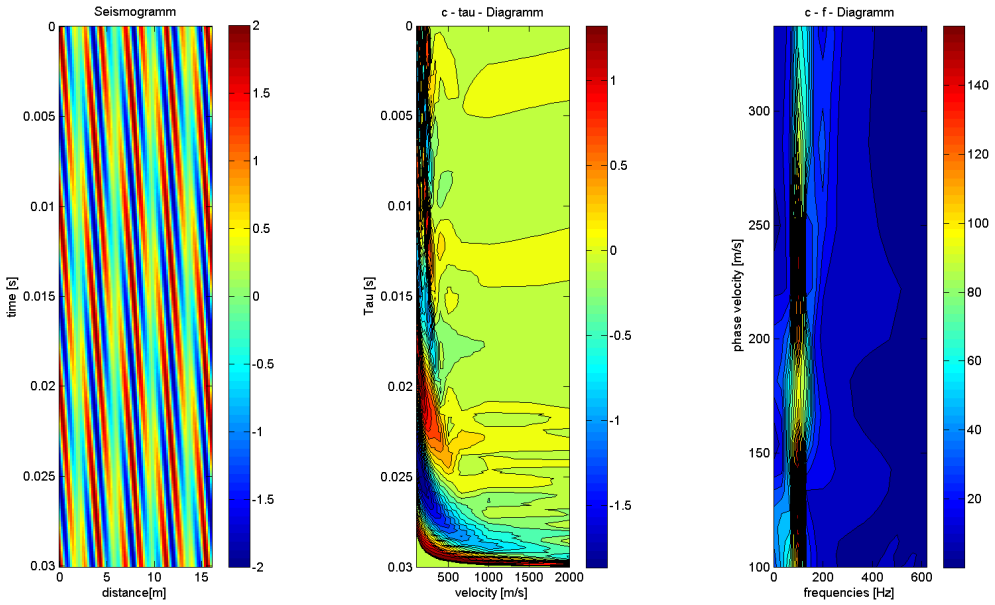

Figure B.4: Image dispersion zoom

$$u(mx, nt) = \begin{bmatrix} x_{11} & x_{12} & x_{13} & \dots & x_{1n} \\ x_{21} & x_{22} & x_{23} & \dots & x_{2n} \\ \vdots & \vdots & \vdots & \ddots & \vdots \\ x_{m1} & x_{m2} & x_{m3} & \dots & x_{mn} \end{bmatrix} \tag{B.8}$$

Therefore the velocity, or slope in which the Radon transform is summing along, is calculated as:

$$v = \frac{skipdistance}{\Delta t} \tag{B.9}$$

where the skip distance is the distance between two receivers(fixed), and Δt is the time-difference between two recorded values of an array; for example, referring to the matrix(B.8):

$$\Delta t_1 = t(x_{22}) - t(x_{11}) \tag{B.10}$$
$$\Delta t_2 = t(x_{23}) - t(x_{11}) \tag{B.11}$$
$$\Delta t_d = t(x_{2d}) - t(x_{11}) \tag{B.12}$$
$$\tag{B.13}$$

Thus the values of the velocity, calculated by eq. (B.9), will be discrete due to the discrete value of the time domain: each time point is shifted from the preceding by the period $T = \frac{1}{f_s}$.

$$v_1 = \frac{skipdistance}{\Delta t_1} \tag{B.14}$$
$$v_2 = \frac{skipdistance}{\Delta t_2} \tag{B.15}$$
$$v_d = \frac{skipdistance}{\Delta t_d} \tag{B.16}$$
$$v_{d+1} = \frac{skipdistance}{\Delta t_{d+1}} \tag{B.17}$$
$$\tag{B.18}$$

Moreover, the discrete velocity domain does not increase linearly; in fact if the difference between two next discrete velocities is calculated it can be seen that:

$$v_1 - v_2 = \Delta v_1 \tag{B.19}$$
$$v_d - v_{d+1} = \Delta v_2 \tag{B.20}$$
$$\Delta v_1 >> \Delta v_2 \tag{B.21}$$
$$\tag{B.22}$$

where d($3 < d < N - 1$) represents the indices of the time discrete value in the matrix (B.8).

Step three - $\tau - p$ Transform. This last step considers the same model shown in step 2 with the difference that in this case both layers are thought as damping materials. This permits to see another limit of the $\tau - p$ transform. Wave propagation are calculated using the same parameters as in step two (either in one), the difference being in the attenuation coefficients β, β_1, β_2 that in this case will be set to a value different from zero.
In this paragraph the calculation of the time delays and velocities will be not repeated, as they have been already explained in step 2. Referring to the previous chapter, let's define the parameters:

- force frequency input $f = 100$ Hz
- skip distance $dx = 0,2$ m

- thickness layer one $z_1 = 0.1$ m,
- thickness layer two $z_2 = 0.15$ m,
- propagation velocity of layer one $v_1 = 140$ m/s
- propagation velocity of layer two $v_2 = 220$ m/s
- damping factor layer one and two $\beta = \beta_1 = \beta_2 = 200$

The sound propagation can be calculated, referring to the hypotesis (H.1), with the eq. (B.6). The result is shown in B.5.

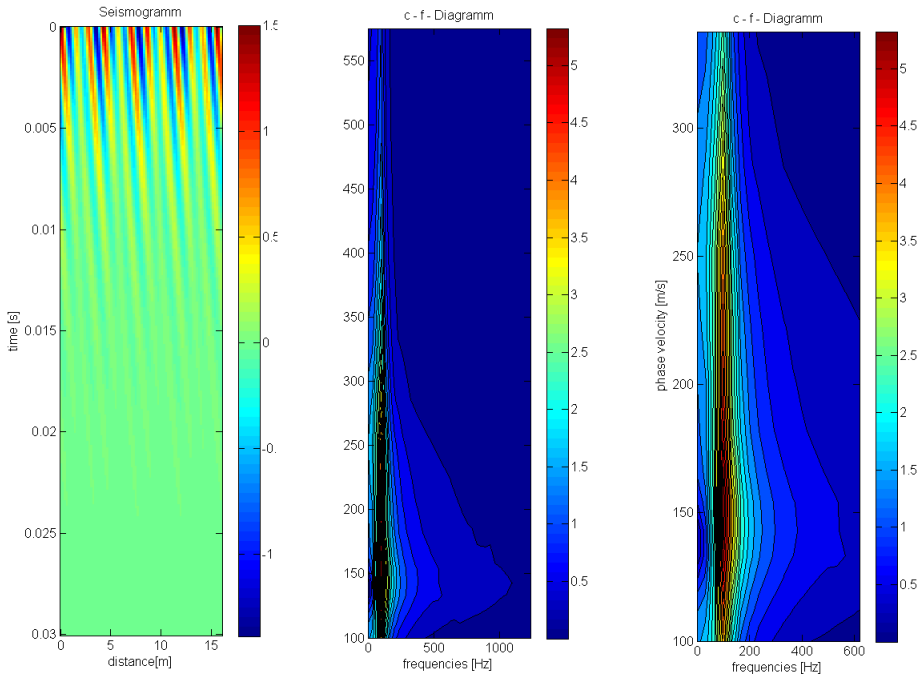

Figure B.5: Signal imagine, Phase shift image dispersion, Zoomed phase shift image

As it can be seen on the right side of Fig. B.2, this time the velocities v_1 and v_2 are not separated from each other at the frequency of 100 Hz. Despite the step before, the resolution of the image dispersion now is not well defined. The problem comes from the fact that the amplitude in this case is attenuated by a coefficient $\beta = 200$, so that, when the transformation is calculated for a velocity of 220 m/s, the amplitude does not reach a relative maximum.

Step three - Phase-shift method. At this case also the phase shift method has been applied, in order to see which method does have the better resolution. The result obtained by the phase shift method is shown in Fig. B.6. As it can be a better resolution is obtained, and the two velocities are well defined. The better resolution is due to the fact that the phase shift method doesn't take into account the amplitude of the signal, so the limit seen for the $\tau - p$ transform can be avoided. For this reason the phase shift method seems to be a better image dispersion process, for finding out the dispersion curve.

B.1.2 Conclusion

Comparing the $\tau - p$ transform and the phase shift method, it has been found that a better resolution of the dispersion curves can be provided using the phase shift method. Of course this method too has limitations, which are not discussed in this paper, due to the aliasing that at low velocities can yield problems in identifying the right velocity propagation. Moreover, when this method is applied to a medium with a high reflection, for example a dense asphalt pavement, it could be difficult to provide the right phase velocity due to the aliasing again.

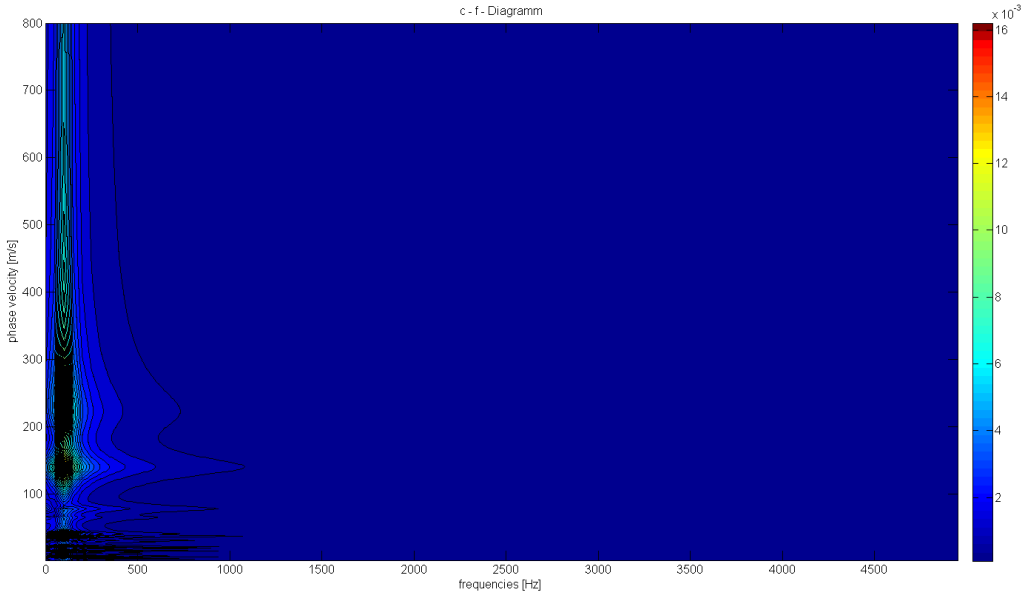

(a) Image dispersion of a testing signal

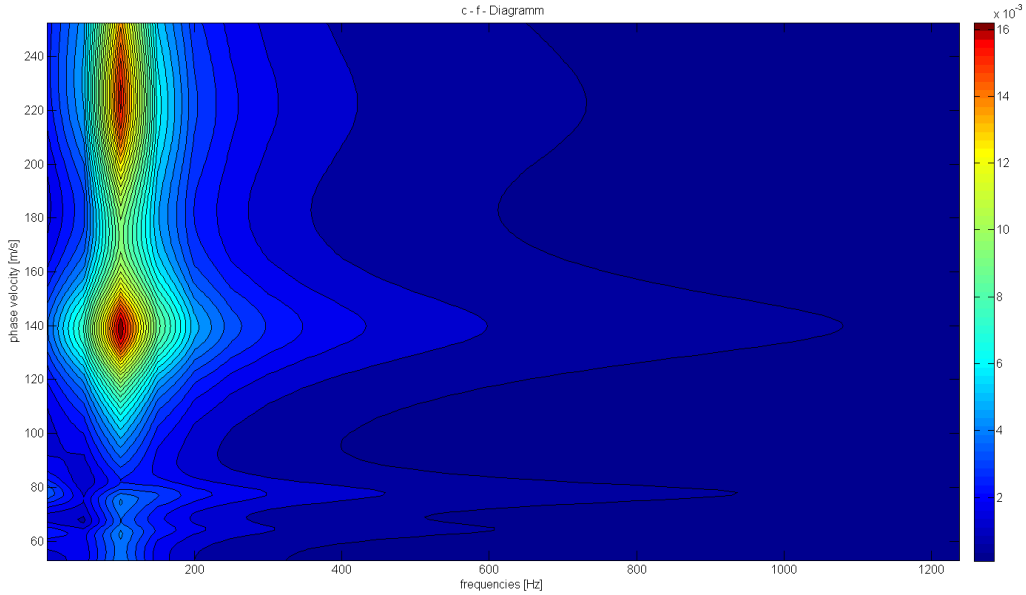

(b) Zoomed Image dispersion of a testing signal

Figure B.6: Phase shift image dispersion

Bibliography

[1] J. W. Strutt, L. Rayleigh *The theory of sound*,Mac Millan and co., Volume I, January 1877.

[2] F. G. Leppington, E. G. Broadbent, and K. H. Heron, The acoustic Radiation Efficency of Rectangular Panels,The Royal Society **382**(1783), pp.245-488, August 1982.

[3] L. Cremer, M. Heckl, E. E. Ungar *Structure-Borne Sound*, Springer, Volume I, January 2005.

[4] F.Fahy, P.Gardonio *Sound and structural vibration*, Academic Press, Volume I, December 2006.

[5] C. E. Wallace, Radiation Resistance of a Rectangular Panel, Journal of the Acoustical Society of America, **51**(3B), pp.946, April 1972.

[6] N. Hashimoto, Measurement of sound radiation efficiency by the discrete calculation method, Applied Acoustics **62**(4), pp. 429-446, March 2001.

[7] G. Maidanik, Response of ribbed panels to reverberant acoustic fields, Journal of Acoustical Society of America, **34**(6), pp.809, June 1962.

[8] C. Guigou-Carter , M. Villot, R. Wetta, Prediction method adapted to wood frame lightweight constructions, Building Acoustics **13**(3), pp. 173–188, September 2006.

[9] EN ISO 10848-1:2006. Acoustics – Laboratory measurement of the flanking transmission of airborne and impact sound between adjoining - Part 1: Frame document, Switzerland.

[10] R. Giannetti, A. Petrella, J. Bach, and A. Silverman, Feasibility study of in vivo bone depth measurement using high frequency ultrasound, Proc. of IEEE International, Instrumentation and Measurement Technology Conference (I2MTC), pp. 762–766, May 2015.

[11] J. H. Kurz, C. U. Grosse, and H.-W. Reinhardt, Strategies for reliable automatic onset time picking of acoustic emissions and of ultrasound signals in concrete, Ultrasonics **43**(7), pp. 538 – 546, June 2005.

[12] G. Robles, J. M. Fresno, and R. Giannetti, Ultrasonic bone localization algorithm based on time-series cumulative kurtosis, ISA Transaction **66**(1), pp.469-475, January 2017.

[13] C. B. Park, Imaging Dispersion of MASW Data—Full vs. Selective Offset Scheme, Journal of Environmental and Engineering Geophysics **16**(1) pp. 13–23, March 2011.

[14] G. Beylkin, Discrete Radon Transform, IEEE International, Proc of Transaction on acoustic, speech, and signal processing **35**(2), pp.162-172 ,February 1987.

[15] J. M. Fresno, R. Giannetti, G. Robles, A survey of time-of-flight algorithm to determinate bone position, Proc. of IEEE International, Instrumentation and Measurement Technology Conference (I2MTC), pp.335-340, May 2017.

[16] M. Möser, *Engineering Acoustics: An introduction of noise control*, Springer, Volume I, January 2009.

[17] C. Park, R. D. Miller, J .Xia, Imaging dispersion curves of surface waves on multi-channel record, Society of Exploration Geophysicists **10**(1) pp.1377-1380, January 1998.

[18] J.Berthaut, M.N Ichchou, L.Jezequel, K-space identification of apparent structural behaviour, Journal of Sound and Vibration **280**(5), pp. 1125-1131, February 2005.

[19] G. A. McMechan and M. J. Yedlin, Analysis of dispersive wave by wavefield transformation, Geophysics **46**(6) , pp.869-874, June 1981.

[20] N.A.Haskell, The dispersion of surface waves on multilayared media, Bulletin of the Seismological Society of America, **43**(1), pp. 17-34, January 1953.

[21] C. Park, R. D. Miller, J. Xia, Multichannel Analysis of Surface Waves, Geophysics **60**(3) , pp.800-808, May 1999.

[22] R. Schultz, Y. J. Gu, Flexible, inversion based Matlab implementation of the Radon transform, Computer and geosciences **52**(1), pp.437-442, March 2013.

[23] N. A. Haskell, The dispersion of surface waves on multilayared media, Bulletin of the Seismological Society of America **43**(1), pp. 17-34, January 1953.

[24] D.Scheibner, T. Park, Slowness aliasing in the Radon transform, Proc. of IEEE International Conference, Acoustics Speech and Signal Processing (ICASSP), March 1984.

[25] M. N. Ichchou, O. Bareille, J. Berthaut, Identification of effective sandwich structural properties via an inverse wave approach, Engineering Structures **30**(10),pp 2591—2604, October 2008.

[26] M. N. Ichchou, O. Bareille, J. Berthaut, The prediction of flanking sound transmission below the critical frequency, The Journal of the Acoustical Society of America **132**(2359),pp 2359—2370, July 2012.